Development of The Low Momentum Track Reconstruction Program and The Kinematic Fitter for The BELLE Experiment

JUN-ICHI TANAKA

Department of Physics, University of Tokyo

January 12, 1999

Abstract

I have developed a low momentum track reconstruction program to mainly improve the reconstruction efficiency of slow π form the D^* decay. It is important to achieve a good reconstruction efficiency of D^* since $B \to D^{*+}D^{*-}$ decay is one of decay mode in which CP violation can be measured in the BELLE. Reconstruction efficiency of $D*$ is improved by 36% by introducing the low momentum track reconstruction. I also have developed kinematic fitters to obtain vertices of particles such as B mesons and improve momentum resolution. A determination of vertices are essential for the the measurement of the CP violation in the BELLE.

Contents

List of Tables

List of Figures

Chapter 1

Introduction

1.1 Introduction

A major unresolved issue is how the current Universe, which is composed entirely of matter, evolved from the matter-antimatter symmetric Big Bang. The CP violation has played a key role in the development of the Universe.

Kobayashi-Masukawa theory[1], which is one foundation of the Standard Model, was introduced to describe an origin of the violation of the CP symmetry. Kobayashi and Masukawa described the CP violation within the Standard Model by introducing third generation of quarks. Sanda and Carter[2] pointed out that the large CP violation can be observed in the B meson decays. The BELLE experiment[3] at KEK[1] is being constructed to observe the CP violation in B decays.

The CP violation can be observed in decay modes such as $B \rightarrow J/\Psi K_S$, $B \rightarrow D^* D^*$, and $B \rightarrow \pi\pi$. Low P_t track reconstruction is very important to observe the CP violation in the $B \rightarrow D^{*+} D^{*-}$ decay since D^{*+} decays into D^0 and π^+, and the pion momentum is very low($<\sim$ 200 MeV/c) due to small Q-value of the decay. I have developed a low P_t track reconstruction program to increase the reconstruction efficiency of the slow π from the D^{*+} decay.

Measurement of the B decay vertex is crucial to observe the CP violation in the BELLE as explained in the following sections. Improvement of the S/N ratio is important in our interesting decay modes such as $B \rightarrow D^{*+} D^{*-}$ since their branching ratio(BR) is small($10^{-5 \sim 7}$). I have developed a kinematic fitter which can calculate decay vertices of B etc. and can improve S/N ratio.

[1] High Energy Accelerator Research Organization at Japan

1.2 B Physics

1.2.1 CP Violation and Neutral K Meson

The parity(P) transformation changes the sign of the spatial coordinate and does not change the sign of the time coordinate:

$$x = (t, \boldsymbol{a}) \xrightarrow{P} x_P = (t, -\boldsymbol{a}).$$

The charge conjugation(C) transformation exchanges particle and anti-particle. These P and C transformations do not violate a symmetry in the strong interaction and electro-magnetic interaction, however, violate it in the weak interaction. The combination of C and P transformations had been considered to keep a symmetry in the weak interaction.

The flavor eigenstates of the neutral K meson are K^0 and its anti-particle $\overline{K^0}$:

$$CP|K^0\rangle = |\overline{K^0}\rangle.$$

This is not a CP eigenstate. Newly, $|K_1^0\rangle$ and $|K_2^0\rangle$ are defines as,

$$|K_1^0\rangle = \frac{1}{\sqrt{2}}(|K^0\rangle + |\overline{K^0}\rangle), \ \ |K_2^0\rangle = \frac{1}{\sqrt{2}}(|K^0\rangle - |\overline{K^0}\rangle).$$

From it,

$$CP|K_1^0\rangle = +|K_1^0\rangle, \ \ CP|K_2^0\rangle = -|K_2^0\rangle.$$

CP eigenstates can be created from the new definition.

The neutral K meson decays to $\pi^+\pi^-$ or $\pi^+\pi^-\pi^0$. Since a spin of the neutral K meson is 0, the system of 2π is $CP = +1$ and that of 3π is $CP = -1$. If the CP symmetry is conserved, always $K_1^0(CP = +1)$ decays to 2π and $K_2^0(CP = -1)$ decays to 3π. In these decays, the phase space of the 2π decay is larger than that of 3π. Because of this, a life time of K_1^0 is shorter than that of K_2^0. K_1^0 is called K_S and K_2^0 is called K_L. However, Christenson *et al.*[4] found $K_L \to 2\pi$ in 1964, that is, CP violation.

1.2.2 Kobayashi – Masukawa Theory and Unitarity Triangle

To describe the CP violation within the Standard Model, Kobayashi and Masukawa introduced an existence of the 3 generation quarks and a 3×3 matrix to mix these quarks [2] in 1973. This matrix is called CKM matrix and the complex phase of it is a source of the CP violation.

[2]This is an extension of 2×2 Cabbibo matrix.

In the original thesis of Kobayashi and Masukawa, CKM matrix (V) is represented using three angle parameters ($\theta_1, \theta_2, \theta_3$), and one complex phase parameter ($e^{i\delta}$) :

$$\begin{aligned}
\begin{pmatrix} d' \\ s' \\ b' \end{pmatrix} &= V \begin{pmatrix} d \\ s \\ b \end{pmatrix}, && (1.1)\\
V &= \begin{pmatrix} V_{ud} & V_{us} & V_{ub} \\ V_{cd} & V_{cs} & V_{cb} \\ V_{td} & V_{ts} & V_{tb} \end{pmatrix} && (1.2)\\
&= \begin{pmatrix} c_1 & -s_1c_3 & -s_1s_3 \\ s_1c_2 & c_1c_2c_3 - s_2s_3e^{i\delta} & c_1c_2s_3 + s_2c_3e^{i\delta} \\ s_1s_2 & c_1s_2c_3 + c_2s_3e^{i\delta} & c_1s_2s_3 - c_2s_3e^{i\delta} \end{pmatrix} && (1.3)\\
c_i &= \cos\theta_i, \quad s_i = \sin\theta_i
\end{aligned}$$

The CKM matrix is expanded around the Cabbibo angle $\lambda = \sin\theta_c$ [3] :

$$V = \begin{pmatrix} 1-\lambda^2/2 & \lambda & A\lambda^3(\rho - i\eta) \\ -\lambda & 1-\lambda^2/2 & A\lambda^2 \\ A\lambda^3(1-\rho-i\eta) & -A\lambda^2 & 1 \end{pmatrix} + O(\lambda^4). \quad (1.4)$$

In these 4 parameters (λ, A, ρ, η), λ and A were measured in good precision, however parameters related with the complex phase, ρ and η were not measured, only the relation equation was measured as,

$$\begin{aligned}
\lambda &= \sin\theta_c = 0.221 \pm 0.002,\\
A &= 0.839 \pm 0.041 \pm 0.082,\\
\sqrt{\rho^2+\eta^2} &= 0.36 \pm 0.14.
\end{aligned}$$

Because the CKM matrix is a unitarity matrix, these elements satisfy a following equation,

$$V_{ij}V^*_{ik} = \delta_{jk}.$$

Particularly, an equation of $j = b$, $k = d$ is associated with the neutral B meson decays,

$$V_{td}V^*_{tb} + V_{cd}V^*_{cb} + V_{ud}V^*_{ub} = 0. \quad (1.5)$$

This relation can be represented as a triangle[4], so called unitarity triangle, shown in Figure 1.1.

[3]This method is called the usage of Wolfenstein

[4]Other relations can be represented as triangles. However it is difficult to create a triangle with measurements because one side of the triangle is much smaller than others.

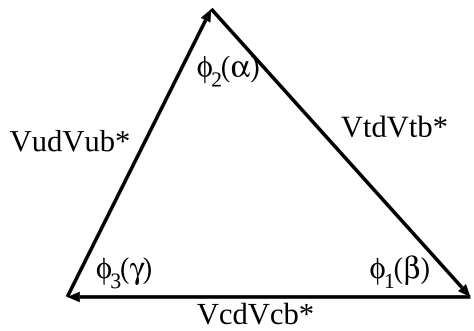

Figure 1.1: Unitarity Triangle

Three angles of this triangle are called the unitatiry angles and are defined as,

$$\phi_1 \equiv \arg\left(\frac{V_{cd}V_{cb}^*}{V_{td}V_{tb}^*}\right), \tag{1.6}$$

$$\phi_2 \equiv \arg\left(\frac{V_{ud}V_{ub}^*}{V_{td}V_{tb}^*}\right), \tag{1.7}$$

$$\phi_3 \equiv \arg\left(\frac{V_{cd}V_{cb}^*}{V_{ud}V_{ub}^*}\right). \tag{1.8}$$

And sometimes these angles are quoted as,

$$\alpha = \phi_2, \quad \beta = \phi_1, \quad \gamma = \phi_3. \tag{1.9}$$

Primary goal of the BELLE experiment is measurement of the angles and the sides of the unitatiry triangle. If it turns out to be consistent with a triangle, it means that Kobayashi-Masukawa theory within the Standard Model is right, however if not, it means that there should be a new physics beyond the current Standard Model.

1.2.3 Determination of ϕ_1

It is important to determine the value of ϕ_1 in the unitary triangle, since it is easier to measure than other values. The $B \to J/\Psi K_S$ decay is the most promising mode since the branching fraction is relatively large ($\sim 10^{-4}$) and the signals is very clean.

$B \to J/\Psi K_S$

$J/\Psi K_S$ is a CP eigenstate [5].

[5] Exactly, K_S is not a CP eigenstate, but the CP violation in the K meson is much small so that it is negligible.

Two contributions are considered in this decay, one is a tree diagram and the other is a penguin diagram.

In case of the tree diagram, as shown in Figure 1.2, the amplitude can be written as,

$$\langle J/\Psi K^0 | B^0 \rangle = V_{cb}^* V_{cs} A_t, \tag{1.10}$$

where A_t is an amplitude except for the elements of the CKM matrix.

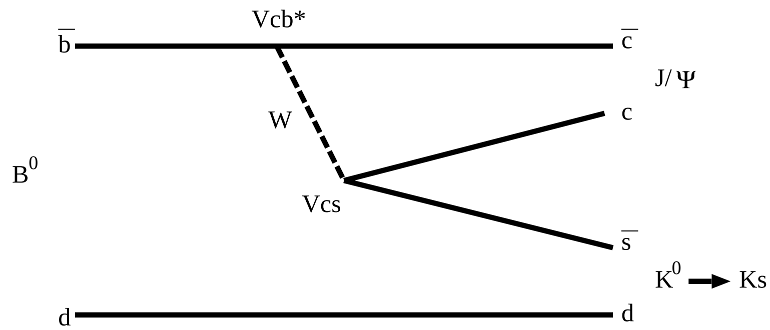

Figure 1.2: Tree Diagram of $b \to c\bar{c}s$

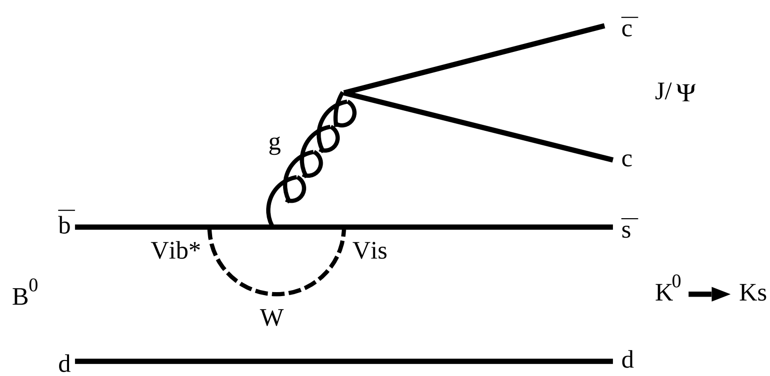

Figure 1.3: Penguin Diagram of $b \to c\bar{c}s$

In case of the penguin diagram, as shown in Figure 1.3, $V_{ib}^* V_{is} (i = u, c, t)$ contributes to this amplitude. But this penguin diagram can be ignored because $V_{cb}^* V_{cs} \cong -V_{tb}^* V_{ts}$ from the relation (1.5) $V_{ib}^* V_{is} = 0$ and $|V_{cb}^* V_{cs}|, |V_{tb}^* V_{ts}| \gg |V_{ub}^* V_{us}|$.

Therefore, in the final state: $J/\Psi K_S$,

$$\begin{aligned}
\langle J/\Psi K_S|B^0\rangle &= \langle K_S|K^0\rangle\langle J/\Psi K^0|B^0\rangle \\
&= \frac{p_K^*}{\sqrt{|p_K|^2+|q_K|^2}} V_{cb}^* V_{cs} A, \\
\langle J/\Psi K_S|\overline{B^0}\rangle & \\
&= \frac{q_K^*}{\sqrt{|p_K|^2+|q_K|^2}} V_{cb} V_{cs}^* A.
\end{aligned} \tag{1.11}$$

From the box diagrams of the neutral K and B meson, $q_{(K)}/p_{(K)}$ can be calculated as follows.

$$\frac{q_K}{p_K} \cong \frac{V_{cd}V_{cs}^*}{V_{cd}^*V_{cs}} \tag{1.12}$$

$$\frac{q}{p} \cong \frac{V_{td}V_{tb}^*}{V_{td}^*V_{tb}} \tag{1.13}$$

Finally, from Equation (A.18), the time dependent CP asymmetry is,

$$\begin{aligned}
Asy\left[J/\Psi K_S;t\right] &= \frac{1}{1+1^2}\left[2\mathrm{Im}\left\{\frac{V_{td}V_{tb}^*}{V_{td}^*V_{tb}}\left(\frac{V_{cd}V_{cs}^*}{V_{cd}^*V_{cs}}\right)^*\frac{V_{cb}V_{cs}^*}{V_{cb}^*V_{cs}}\right\}\sin(\Delta M t)\right. \\
&- \left.(1^2-1)\cos(\Delta M t)\right] \\
&= \sin\left\{\arg\left(\frac{V_{td}V_{tb}^*V_{cd}^*V_{cb}}{V_{td}^*V_{tb}V_{cd}V_{cb}^*}\right)\right\}\sin(\Delta M t) \\
&= \sin\left(\pi-\phi_1+\pi-\phi_1\right)\sin(\Delta M t) \\
&= -\sin(2\phi_1)\sin(\Delta M t).
\end{aligned} \tag{1.14}$$

Other equations to determine ϕ_1 are obtained from Equations (A.14) and (A.15) [6] as follows.

$$\begin{aligned}
\Gamma(B^0(t)\to J/\Psi K_S) &\propto f(t) \text{ or } f(\tau) \\
&= \frac{1}{2}e^{-\Gamma|t|}(1-\sin 2\phi_1 \sin\Delta M t) \\
&= \frac{1}{2}e^{-|\tau|}(1-\sin 2\phi_1 \sin x_d\tau)
\end{aligned} \tag{1.15}$$

$$\begin{aligned}
\Gamma(\overline{B^0}(t)\to J/\Psi K_S) &\propto f(t) \text{ or } f(\tau) \\
&= \frac{1}{2}e^{-\Gamma|t|}(1+\sin 2\phi_1 \sin\Delta M t) \\
&= \frac{1}{2}e^{-|\tau|}(1+\sin 2\phi_1 \sin x_d\tau),
\end{aligned} \tag{1.16}$$

[6] They can prove at $t>0$. At $t<0$, the time evolution factor is $e^{i\gamma_\pm t}$ in Equation (A.8). It can prove at $t<0$.

where $\tau \equiv t\Gamma$[7] and $x_d \equiv \Delta M/\Gamma$. $f(\tau)$ is normalized as,

$$\int_{-\infty}^{\infty} d\tau f(\tau) = 1. \tag{1.17}$$

Equations (1.15) and (1.16) are shown in Figure 1.4. A solid and dashed lines are Equations (1.16) and (1.15), respectively.

When the CP violation does not exist, ϕ_1 is 0, that is, Equation (1.14) is equal to 0 and Equations (1.15) and (1.16) do not have an asymmetry for $\tau = 0$(in Figure 1.4).

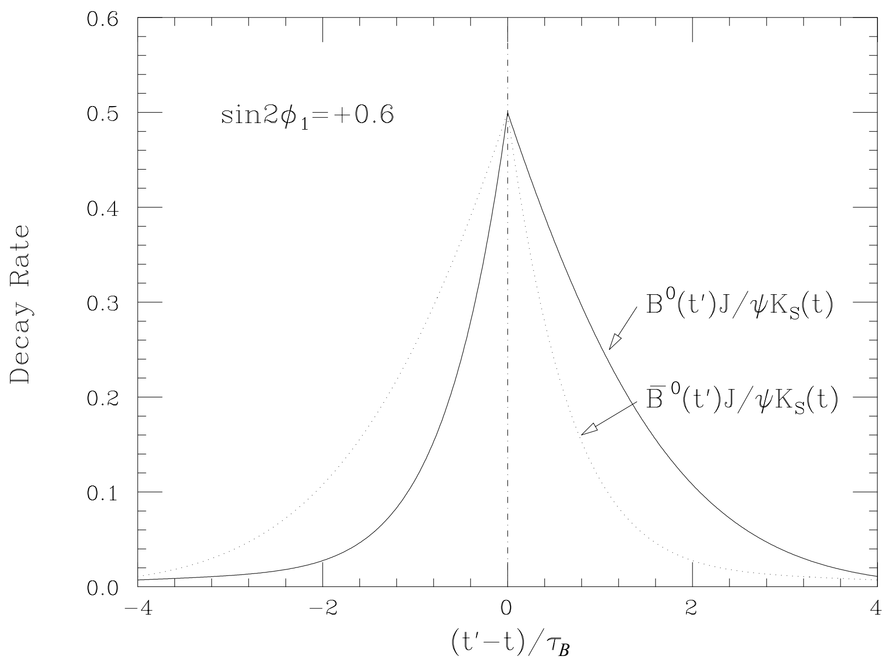

Figure 1.4: Proper time distribution, $t' - t/\tau_B$ corresponds to $\Delta\tau$ in Equation (1.23).

1.2.4 Measurement of ϕ_1

It is necessary to obtain the information of the flavor of B meson and τ in Equations (1.15) or (1.16). Figure 1.5 shows the decay process of $B \to J/\Psi K_S$.

[7] In Appendix A, Γ is written as Γ_0.

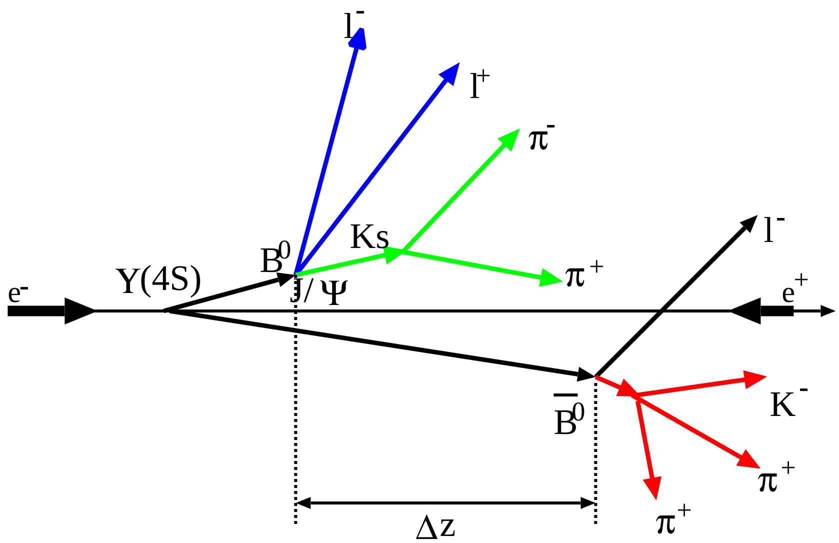

Figure 1.5: An example of the decay process of $B \to J/\Psi K_S$.

Measurement of τ

$\Upsilon(4S)$ decays to B^+B^- or $B^0\overline{B^0}$ with the same probability. Let us consider $\Upsilon(4S) \to B^0\overline{B^0}$. B^0 and $\overline{B^0}$ flight with the $B^0\overline{B^0}$ mixing, however when one decays to some particles as $B^0(\overline{B^0})$, the other have to be $\overline{B^0}(B^0)$ in the same time. So that, a time when $\overline{B^0}$ decays can be selected as the origin of time. In Equation (1.15), t can be written as Δt which is defined as,

$$\Delta t = t_{B^0} - t_{\overline{B^0}},$$

where t_{B^0} and $t_{\overline{B^0}}$ are decay times of B mesons.

When the velocities of two B mesons are v_{B^0} and $v_{\overline{B^0}}$, respectively, Δt can be calculated as,

$$\Delta t = \frac{\Delta l_{B^0}}{v_{B^0}} - \frac{\Delta l_{\overline{B^0}}}{v_{\overline{B^0}}}, \tag{1.18}$$

where Δl_{B^0} and $\Delta l_{\overline{B^0}}$ are the flight length of B mesons, respectively.

In the laboratory frame, the following approximate equations[8] can be obtained because of a large boost factor $\gamma\beta$. This large boost factor is important for the measurement of the CP violation as I describe later.

$$v_{B^0 z} \cong v_{\overline{B^0} z} \tag{1.19}$$

$$v_{B^0 T} \cong v_{\overline{B^0} T} \cong 0 \tag{1.20}$$

[8] $v_{B^0 T}$ is a transverse component of v_{B^0}.

In Equation (1.18), $\Delta l_{B^0} - \Delta l_{\overline{B^0}}$ can be written as,

$$\begin{aligned} \Delta l_{B^0} - \Delta l_{\overline{B^0}} &\cong \Delta z, \\ \Delta z &\equiv z_{B^0} - z_{\overline{B^0}}, \end{aligned} \tag{1.21}$$

where $z_{B^0}(z_{\overline{B^0}})$ is z component of the decay vertex of $B^0(\overline{B^0})$.

From Equations (1.18), (1.19), (1.20), and (1.21),

$$\Delta t \cong \frac{\Delta z}{v_{B^0}}. \tag{1.22}$$

τ can be obtained from Equation (1.22) as,

$$\begin{aligned} \Delta\tau &= \Delta t \Gamma \\ &= \Delta t / \tau_B, \end{aligned} \tag{1.23}$$

where τ_B is a life time of B^0 meson.

Because of a large boost, v_{B^0} can be approximately written as $\gamma\beta c$ of $\Upsilon(4S)$. Therefore, Equation (1.23) can be written as,

$$\Delta\tau \cong \Delta z / \gamma\beta c \tau_B. \tag{1.24}$$

The measurement of Δz is necessary to obtain $\Delta\tau$. The Δz is illustrated in Figure 1.5.

And $\gamma\beta c\tau_B$ indicates that B mesons decay after they flight $\gamma\beta c\tau_B \cong 200\mu$m in the BELLE. If a boost factor is zero, B mesons move by 30μm before their decays and it is not possible to measure Δz. Therefore a large boost factor is important.

Flavor Tagging

B meson which decays to $J/\Psi K_S$ is called B_{CP} and the other B meson is called B_{tag}. And the method of the determination of B_{CP} flavor is called "flavor tagging".

The semileptonic decay of $B_{tag}(b \to cl^- \overline{\nu_l})$ provides one of the methods of the flavor tagging with reasonable efficiency since the charge of lepton(electron and muon) with high momentum indicates the flavor of B_{tag}. In Figure 1.5, it is illustrated as a lepton with negative charge from $\overline{B^0}$. When B_{tag} is $B^0(\overline{B^0})$, a positive(negative) lepton with high momentum can be observed. Therefore if there exists a positive(negative) lepton with high momentum, a B_{CP} flavor is $\overline{B^0}(B^0)$.

The kaon charge also indicates the flavor of B_{tag} since $b \to c \to s$ decay chain is dominant process. In Figure 1.5, it is illustrated as a kaon with negative charge from $\overline{B^0}$.

Good lepton identification and good K/π separation are essential for the flavor tagging.

Chapter 2

BELLE Experiment

2.1 Accelerator

$\Upsilon(4S)$, which is a resonance state of b and $\bar{b}$ quarks, is generated by the collision of electron and position as shown in Figure 2.1.

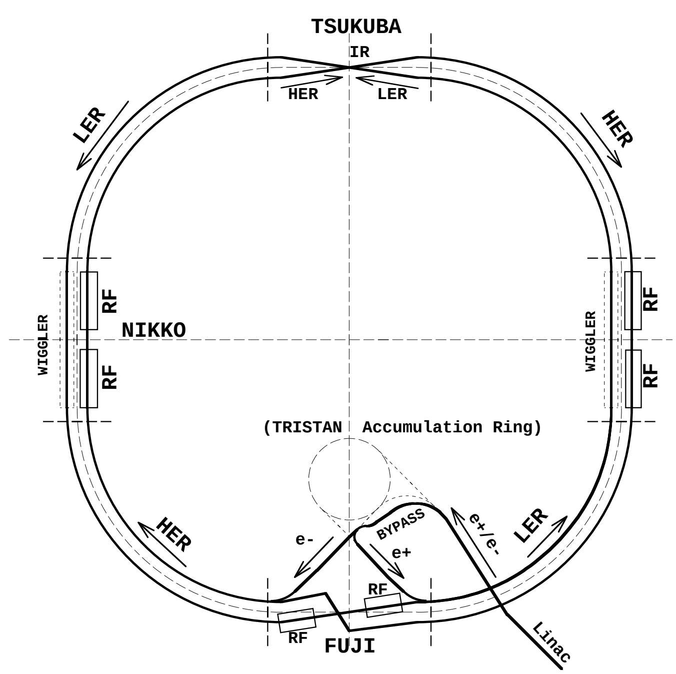

Figure 2.1: KEK Beamline

To give a large momentum to $\Upsilon(4S)$ in the laboratory frame, it is necessary to make beam energy asymmetric, because the measurement of the difference between B meson's vertices becomes more precise. Electron beam energy is 8.0 GeV/c and position beam energy is 3.5 GeV/c [1]. To generate many B mesons, the maximum luminosity is $10^{34} cm^{-2}\,\mathrm{sec}^{-1}$.

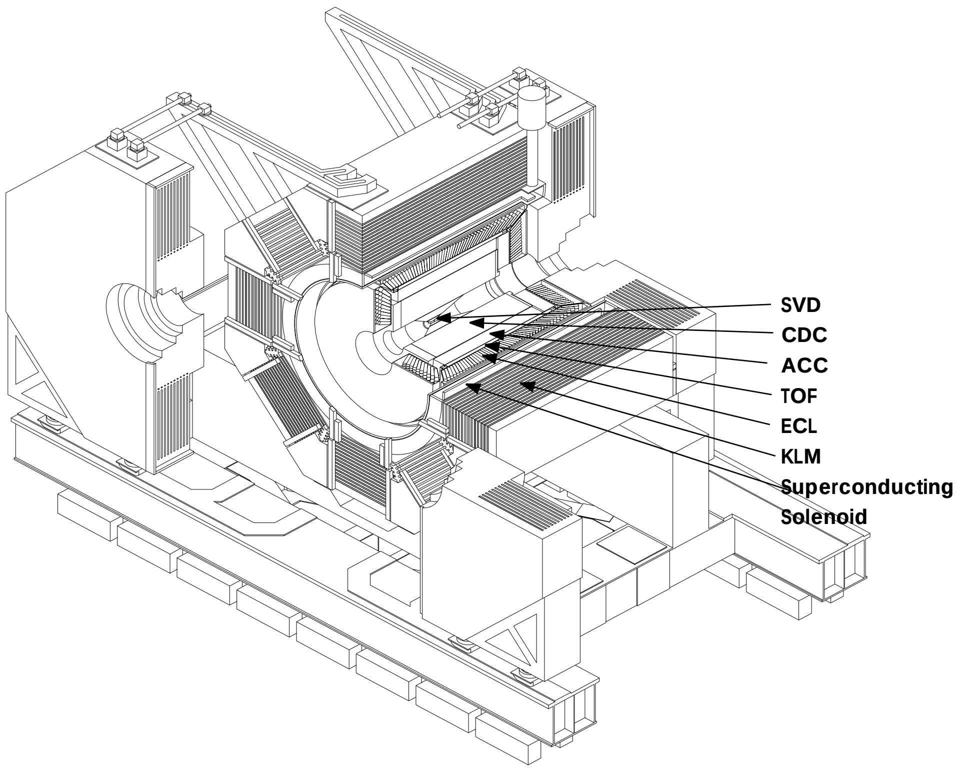

Figure 2.2: BELLE Detectors

2.2 Detector

The structure of BELLE detectors is shown in Figure 2.2. It is asymmetric to its interaction point as shown in Figure 2.3. because the beam energy is asymmetric. The definition of the xyz-axes is shown in Figure 2.4 and z axis is parallel with the beampipe and its + direction is the going direction of the electron beam. xy plane is also called r–ϕ plane as shown in Figure 2.5.

I describe the overview of detectors and then I describe structures of each

[1] In the BELLE, a boost factor $\gamma\beta$ is 0.425.

detector in detail, particularly, the Central Drift Chamber(CDC) since the information from the CDC is used in the section 3.

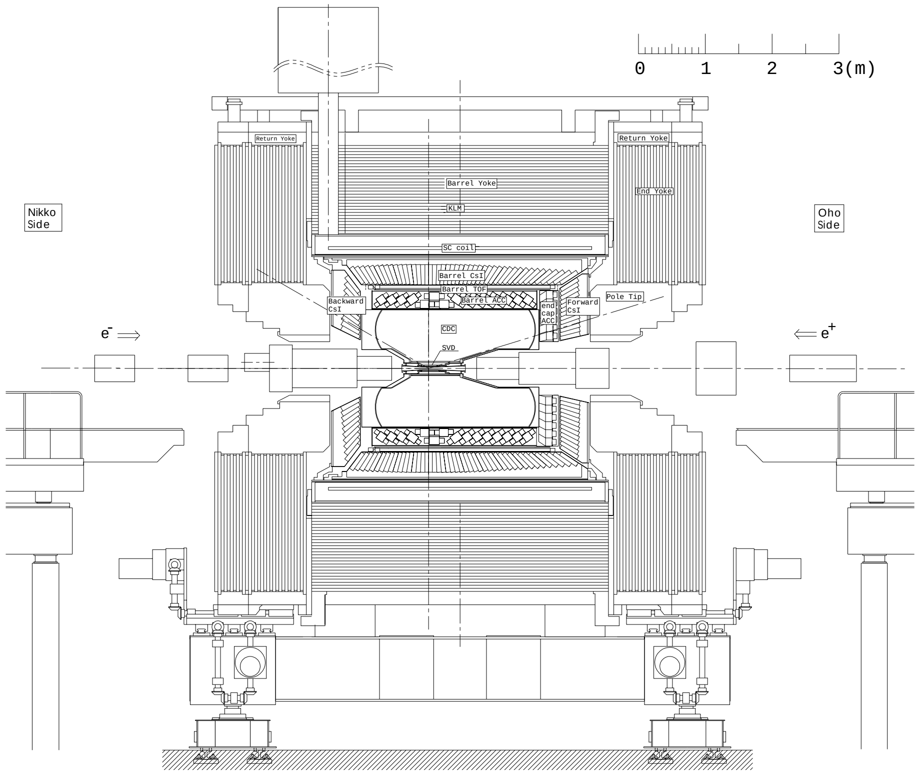

Figure 2.3: Side View of The BELLE Detectors

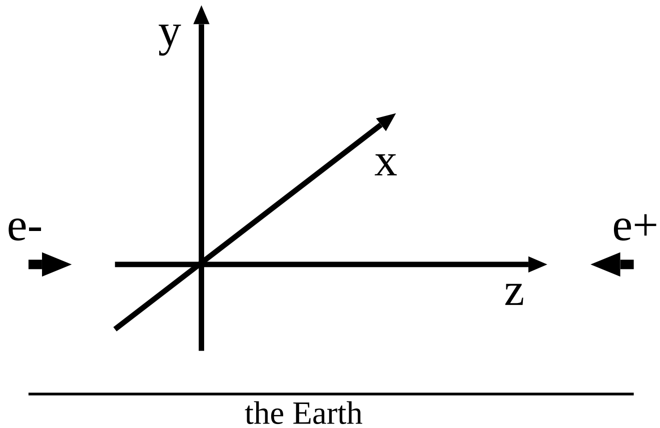

Figure 2.4: The Definition of The Coordinate in The BELLE

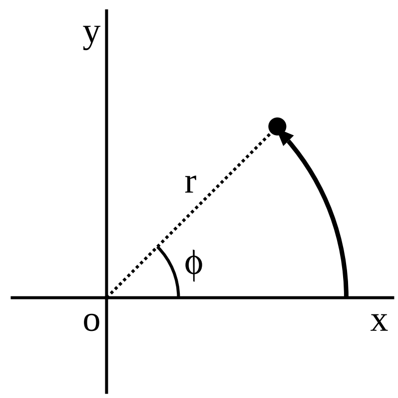

Figure 2.5: The Definition of r–ϕ

2.2.1 Overview

The Silicon Vertex Detector(SVD) which measures vertices is situated just outside of a cylindrical beryllium beampipe. It is important to measure vertices precisely since Δz is necessary to the observation of the CP violation. Outside of the SVD, the CDC is situated, which provides charged particle tracking. And then, the Aerogel Čerenkov Counter(ACC), and the Time of Fight Counter(TOF) are located outside of the CDC. They provide the particle identification, adding dE/dx measurement in the CDC. The particle identification is important to the tagging of B meson flavor which is necessary to the observation of the CP violation. Outside of the TOF, the Electromagmetic Calorimeter(ECL) is situated, which detects electron and γ. The superconducting solenoid is located. It provides about 1.5 Tesla magnetic fields. And outside of it, the K_L/μ Detector(KLM) is situated, which detects K_L and μ.

2.2.2 SVD – Silicon Vertex Detector

The SVD provides measurements of the decay vertices of B mesons for the observation of the CP violation. It is accurate enough to distinguish vertices between decay to the CP eigenstate and tagging decay. The SVD has three layers in Figure 2.6 and Figure 2.7. Each layer provides independent orthogonal two coordinate measurements with its double-sides silicon microstrips. The SVD system's angular coverage is $21° < \theta < 140°$. Δz resolution [2] is about $100\mu m$

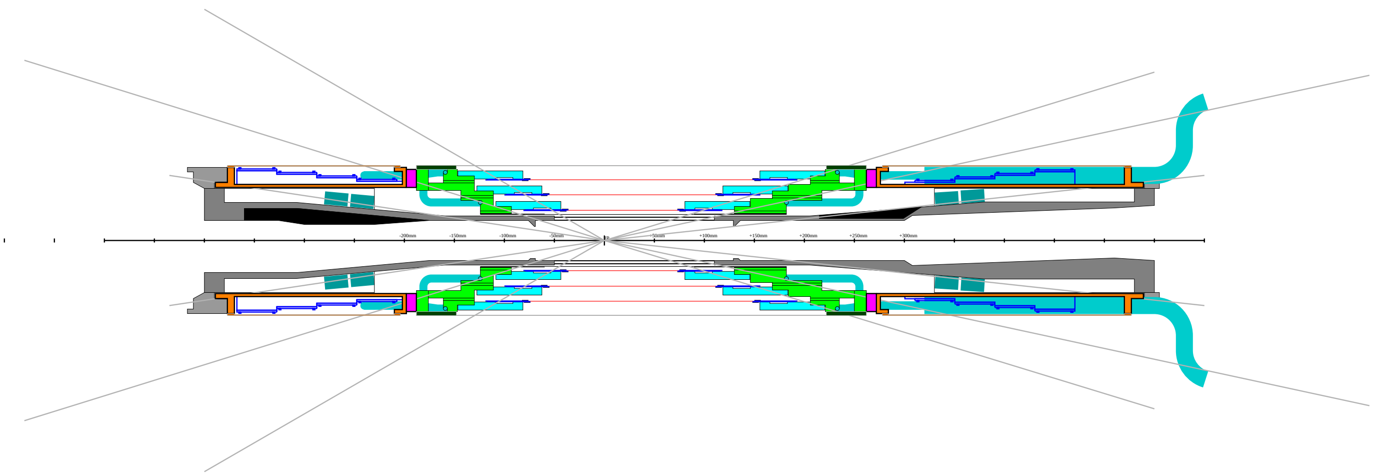

Figure 2.6: Side View of The SVD

[2] It is a vertex of B_{tag} − a vertex of B_{CP}

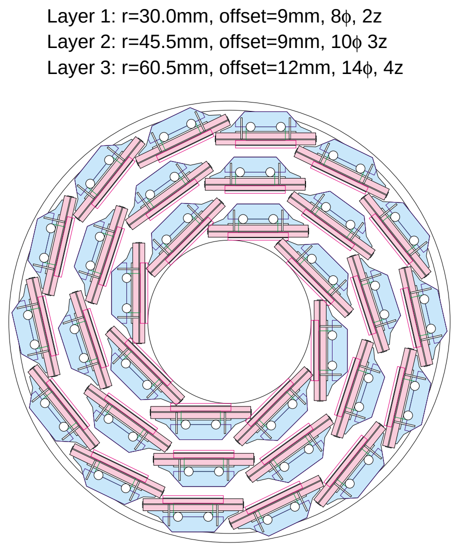

Figure 2.7: Top View of The SVD

2.2.3 CDC – Central Drift Chamber

The CDC provides momentum and energy loss of the charged particles by the reconstruction of these tracks. The information of the reconstructed tracks is the starting point for the particle identification (in the ACC and the TOF) and detection of the electron(in the ECL) and the muon(in the KLM) since reconstructed tracks are extrapolated to the ACC, TOF, ECL and KLM.

Structure

The radius of the most inner part is 8cm, that of the most outer past is 88cm, and the length is 235cm as shown in Figure 2.8. The most inner and outer parts are made by 2mm and 5mm CFRP, respectively. The endplates are made by 10mm Al. The ingredient of the filled gas are helium and ethane and this ratio is 1:1. The CDC system's angular coverage is $17° < \theta < 150°$.

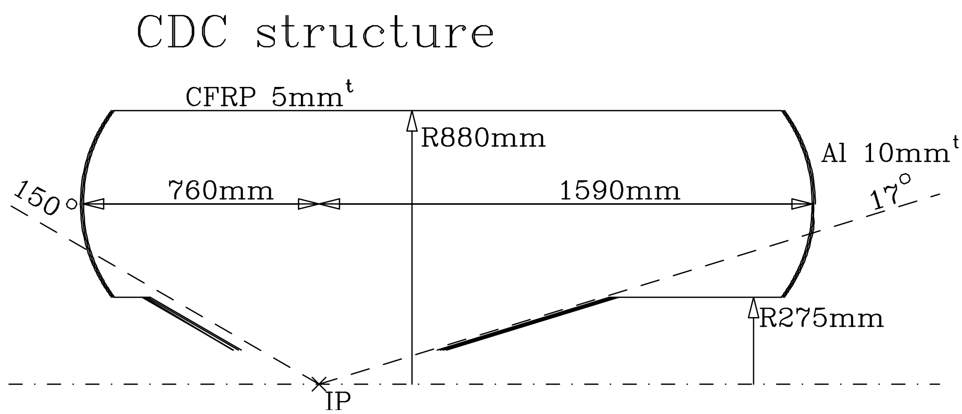

Figure 2.8: Side View of The CDC(upper part: It is a magnified figure of the center of Figure 2.3)

Wire and Layer

The total number of the sense wires are 8400. That of the layers are 50 and cathode parts are 3 layers. These wires are divided to two types, one is an axial wire which is not slant to z axis, the other is a stereo wire which is slant[3]. Similarly, these layers are divided to two types, one is an axial super layer which includes only axial wires and the other is a stereo super layer which includes only stereo wires as shown in Figure 2.9. Wire configuration is shown in Table 2.1. And there are other wires to create cells, that is, 24944 field wires. The size of the cell is about 15mm × 15mm as shown in Figure 2.10.

[3]The slant is about 50 mrad and the number of the axial wires is 5280, that of the stereo wires is 3120.

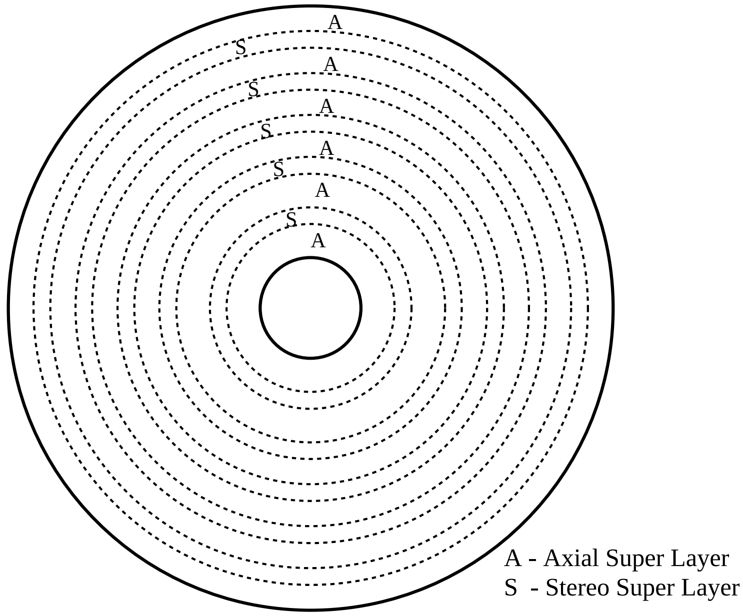

Figure 2.9: R–ϕ View of The CDC

layer type	no. of the layer	wires per one layer	total wires	index of the axial layer	index of the stereo layer	index of the super layer
axial	6	64	384	1	-	1
stereo	3	80	240	-	1	2
axial	6	96	576	2	-	3
stereo	3	128	384	-	2	4
axial	5	144	720	3	-	5
stereo	4	160	640	-	3	6
axial	5	192	960	4	-	7
stereo	4	208	832	-	4	8
axial	5	240	1200	5	-	9
stereo	4	256	1024	-	5	10
axial	5	288	1440	6	-	11

Table 2.1: Sense Wires

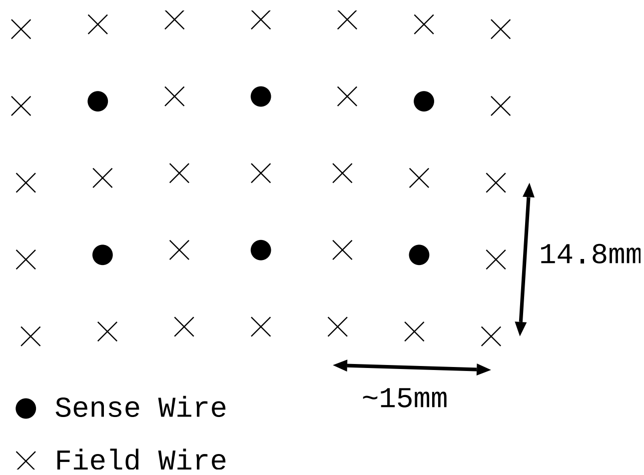

Figure 2.10: Sense and Field Wires

Performance

The performance of the CDC[3][9] are as follows.

1. The spatial resolution is 120μm $\sim$ 150μm.
2. The resolution of ${P_t}^4$ is $\frac{\delta P_t}{P_t} \sim 0.5\%\sqrt{1+P_t^2}$.
3. The resolution of the energy loss dE/dx is $\frac{\delta_{dE/dx}}{dE/dx} \sim 6\%$.

2.2.4 ACC – Aerogel Čerenkov Counter

The ACC identifies particles, that is, K/π separation, with momentum greater than 1.2 GeV/c. Čerenkov radiations occur in case of

$$n \quad > \quad 1/\beta = \sqrt{1+(m/p)^2},$$

where p is a measured momentum value with the CDC and n is the index of refraction.

The ACC, which consists of a single layer of aerogel detectors, is divided into two parts: a barrel array occupying the volume bounded by $88.5 < r < 115$ cm and $-85 < z < 162$ cm, and a forward endcap array occupying the region bounded by $42 < 114$ cm and $166 < z < 194$ cm. These are shown in Figure 2.11 and Figure 2.12.

4 Transverse momentum. A unit of P_t is GeV.

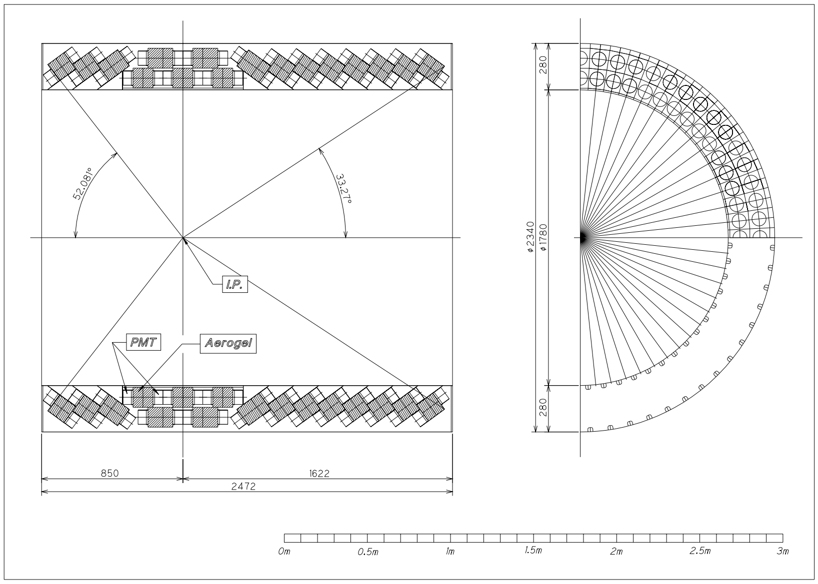

Figure 2.11: Barrel Part of The ACC

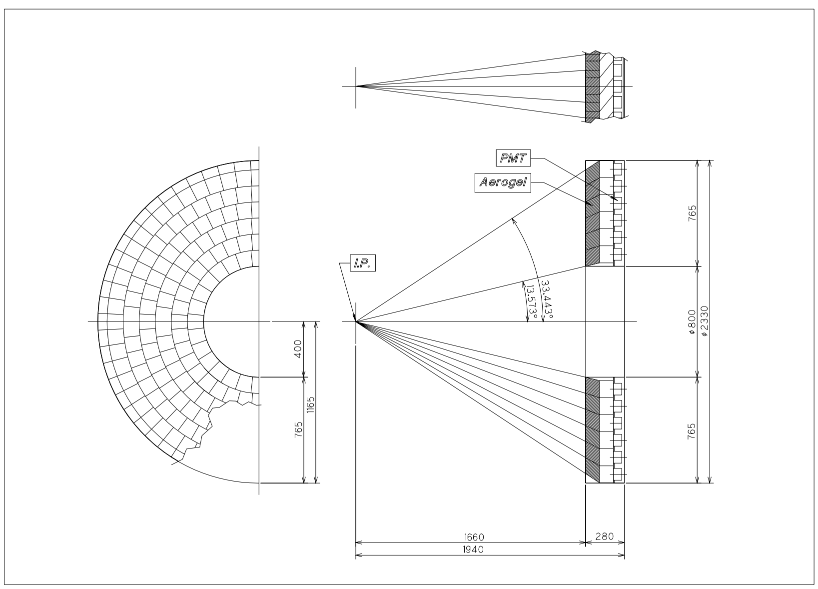

Figure 2.12: Endcap Part of The ACC

2.2.5 TOF – Time of Fight Counter

The TOF provides $3\sigma K/\pi$ separation up to 1.2 GeV/c with a TOF time resolution of 100ps. The following equation is satisfied using a measured time-of-fight T with the TOF and a measured momentum p with the CDC.

$$T = L/c\sqrt{1+(m/p)^2},$$

where L is a length of the fight.

One TOF module is shown in Figure 2.13. It consists two trapezoidally shared TOF counter and one TSC(Thin Scintillation Counter) counter. And 64 modules are mounted in BELLE. The TOF system's angular coverage is $33.7° < \theta < 120.8°$.

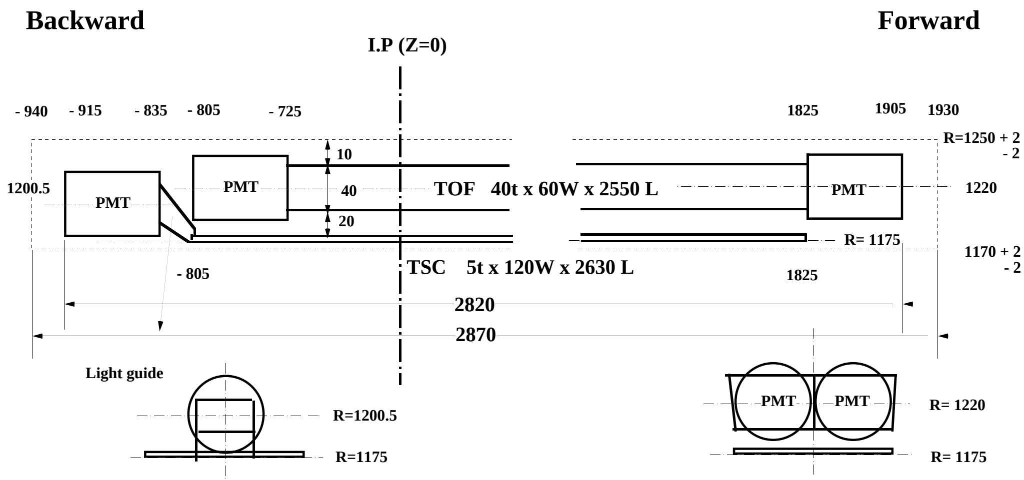

Figure 2.13: A Module of The TOF

2.2.6 ECL – Electromagmetic Calorimeter

The ECL detects γs and electrons using the electromagmetic shower. In case of γ, its energy and position are measured. γ is important to the analysis of π^0 included decays such as $B \to \pi^0\pi^0$. Electron is mainly necessary for the tagging of the CP violation. And in case of electron, its identification is done by comparing its measured momentum with the CDC and its energy deposit on the ECL. For the calorimeter, CsI(Tl) crystal is chosen. Its typical size is around 6cm $\times$ 6cm $\times$ 30cm. The ECL consists of 3 parts: a barrel part, whose angular coverage is $32.2° < \theta < 128.7°$ with 6624 crystals, and a forward endcap, $12.4° < \theta < 31.4°$ with 1152 crystals, and a backward endcap, $130.7° < \theta < 155.0°$ with 960 crystals.

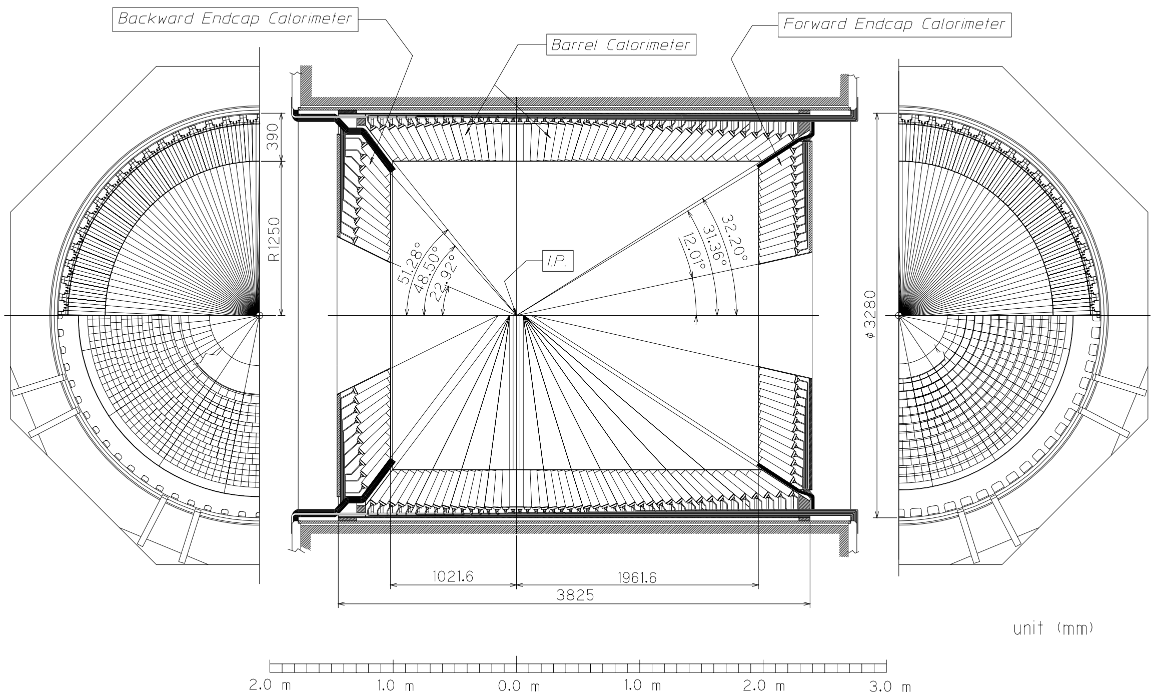

Figure 2.14: Barrel and Endcap Parts of The ECL

2.2.7 Superconducting Solenoid

The superconducting solenoid provides a magnetic field of about 1.5T(Tesla) in a cylindrical volume of 3.4m in diameter and 4.4m in length. It is not uniform field and distorted field a little.

2.2.8 KLM – K_L/μ Detector

The KLM detects K_L and μ and measures their positions. K_L is necessary to the analysis of K_L included decays such as $B \to J/\Psi K_L$ from which the CP violation can be measured. μ is mainly necessary for the tagging of the CP violation. It consists of octagonal barrel and two endcaps which are a sandwich structure of 14 iron plates of 4.4cm thick and 14(15 for barrel part) layers of 4.7cm thick RPC(Resistive Plate Counter). The KLM system's angular coverage is $25° < \theta < 145°$. In case of K_L, the hadron shower occurs in its iron plates, however in case of μ, it does not occur.

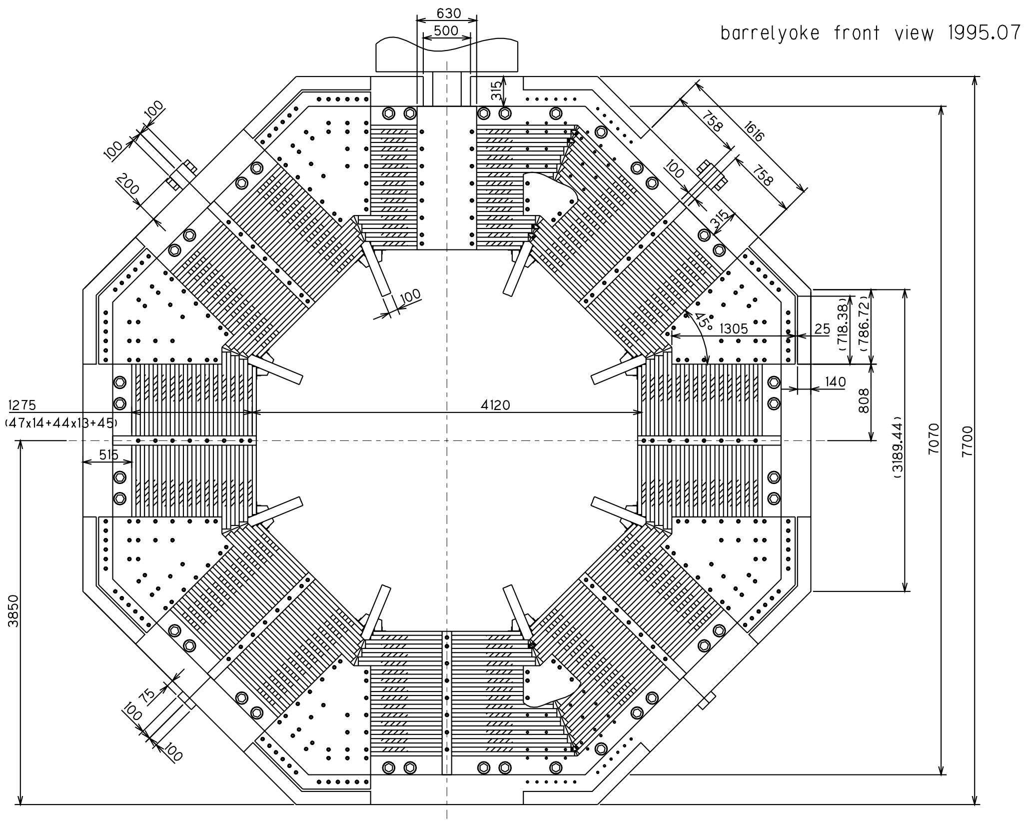

Figure 2.15: Side View of The KLM

Chapter 3

Development of The Low Momentum Track Reconstruction Program

3.1 Overview

The tracking program reconstructs trajectories of charged particles in a magnetic field. A curvature of each trajectory gives a momentum of the charged particle. Since all of other reconstruction tools for the charged track depend on the tracking information, the tracking program plays a crucial role in the BELLE reconstruction program.

In the tracking program, tracks are found in the r–ϕ plane using only axial wires first, and then reconstructed in the three dimensional space using stereo wires ("stereo finder"). Tracks are found mainly by a "conformal finder". In the conformal finder, hit position (x, y) is transformed into (X, Y) by the conformal transformation as,

$$X = \frac{2x}{x^2 + y^2}, \qquad Y = \frac{2y}{x^2 + y^2}.$$

By the conformal transformation, a circle which passes through the origin $(0, 0)$ is transformed into a line. The inverse of the distance of the line from the origin in the conformal plane corresponds to a radius of the circle as shown in Figure 3.1.

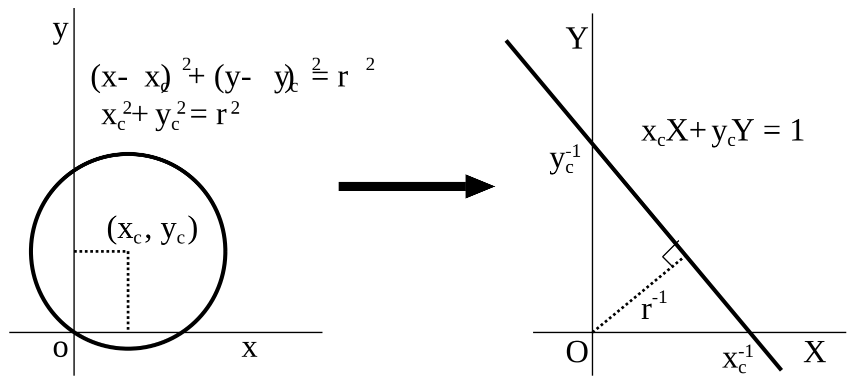

Figure 3.1: Conformal Transformation

The conformal finder finds tracks by searching hits with similar $\phi = tan^{-1}\frac{Y}{X}$ values to achieve fast reconstruction speed. In this method, the efficiency to find tracks degrades with lower transverse momentum (P_t) tracks since r^{-1} become too large. Therefore it is difficult to find tracks with $P_t < 100\mathrm{MeV}/c$ by the conformal finder.

I developed a “curl finder” and an associated stereo finder to find those low P_t tracks not found by the conformal finder. The curl finder ignores axial hits used to reconstruct tracks already found by the conformal finder. However, all stereo hits are used for the three dimensional reconstruction to improve the efficiency since a lack of stereo hits is a main source of inefficiency for low P_t tracks. Figure 3.2 illustrates the difference between tracks found by the conformal finder and the curl finder. The dashed and solid line indicate tracks found by the conformal finder and the curl finder, respectively. As I mentioned above, the low P_t track reconstruction is particularly important for physics analysis which involves D^{*+}, such as $B^0 \to D^{*+}D^{*-}$. In this chapter, the curl finder and the associated stereo finder are described in detail.

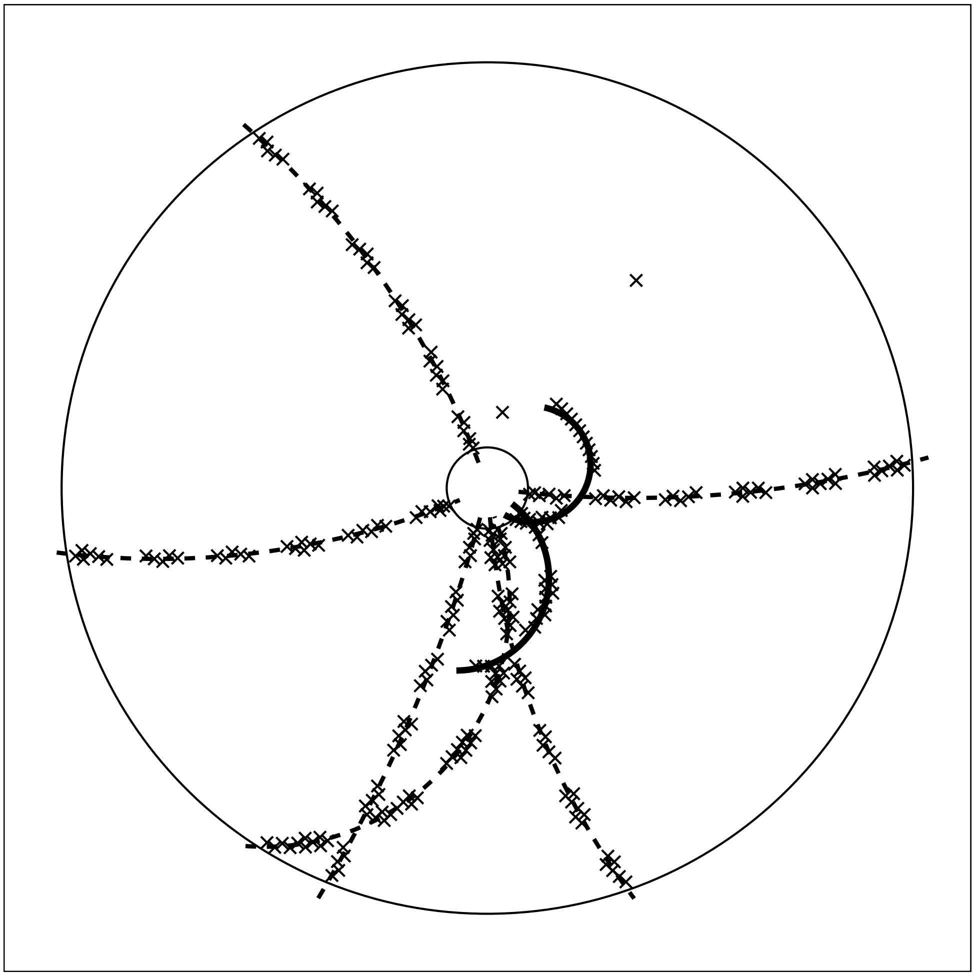

Figure 3.2: Reconstructed tracks in the CDC. Dashed line indicates tracks reconstructed by the conformal finder and solid line indicates tracks reconstructed by the curl finder. Cross marks represent axial hit wires. Stereo hit wires are not shown.

3.2 Curl Finder

The curl finder is designed to reconstruct low P_t charged tracks (50MeV< P_t <200MeV). Those tracks are reconstructed as a circle in the r–ϕ plane unlike the conformal finder. Figure 3.3 shows an example of a low P_t track. The curl finder finds tracks by appending hit wires to "segments" which consists of consecutive hit wires in the same super layer. A special treatment is made to break up segments which consists of two tracks. The segment with the largest number of consecutive hit wires in one layer is used as the first seed segment since hit wires remain as a segment which has consecutive hit wires in one layer and the characteristic can not be in the high P_t track but be in the low P_t track. And hit wires in segments are appended to the seed segment if they are close to the circle which is calculated from the seed segment. And then a track is reconstructed in the r–ϕ plane from the seed segment and its appended hit wires.

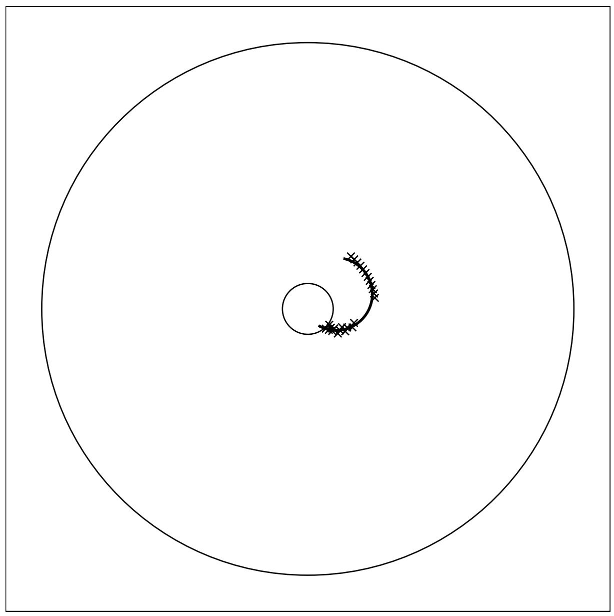

Figure 3.3: A Curling Track in The CDC

A segment is created by collecting neighboring hit wires within a super layer. Figure 3.4 shows an example of the method how to find a segment. The segment finding can start from any hit wire. When there is a neighboring hit wire, it moves to the neighboring hit wire. When there are more than one neighboring hit wires, it move to one of them and the others are marked as "stocked seed wire". When it cannot find any neighboring hit wire, it moves to one of stocked seed wires and repeats the process. When it depletes all of the stock seed wires, the segment is found. If the segment includes less than three hit wires, it is discarded.

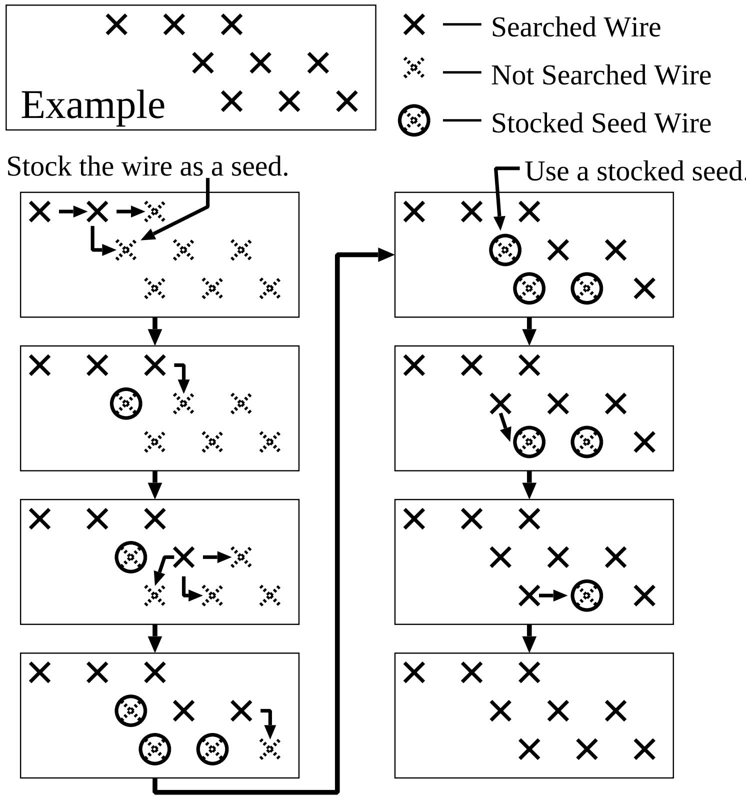

Figure 3.4: An example of the segment finding.

Figures 3.5 and 3.6 show an example of the segment. One track originates from the interaction point(IP), however the other track comes from outside, which can be caused by back scattering from the calorimeter etc.

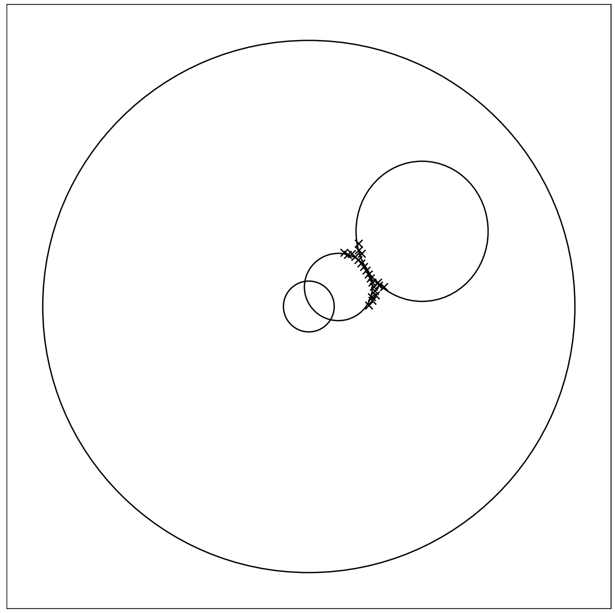

Figure 3.5: A segment in the CDC. One track originates from the interaction point however the other track comes from outside, which can be caused by back scattering from the calorimeter etc.

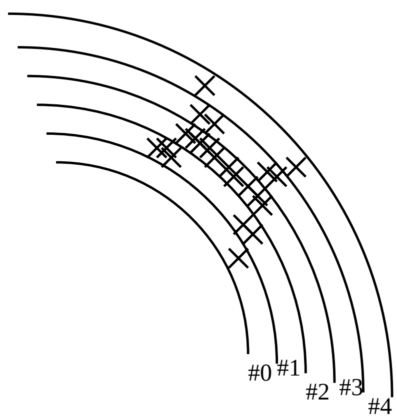

Figure 3.6: A magnified segment of Figure 3.5.

A segment is divided by the layer whose number of consecutive hit wires is the largest in the segment. In the example, the layer #2 includes 10 consecutive hit wires, and the hit wires in layer #3 and #4 are discard since tracks are expected to come from inside. When the largest number of the consecutive hits in a layer is less than 6, this treatment is not made.

A seed segment is selected based on the largest number of consecutive hit wire in one layer. Circle parameters are calculated from wire positions in the seed segment. Drift distance is not included in the calculation currently to save CPU time. Hit wires in segments are appended to the seed segment if a distance of the wire position from the circle is less than 8cm, and the circle parameters are recalculated. After all hit wires in segments are examined, the circle parameter may be recalculated with an IP constraint to improve the calculation. The IP constraint is necessary when the number of wires in the circle is less than 5 and the distance between the circle and the IP is less than 10cm. In the IP constraint, $(0,0)$ is treated as a wire in the fit of the circle. Hit wires which are not included in segments are also appended if the distance of the wire position from the circle is less than 5cm to further improve the fit. After all hits are examined, the circle with less than 5 hit wires is discarded.

Two tracks, positive and negative tracks, can be reconstructed from one circle since it is difficult to determine the charge of the curling track in the $r--\phi$ plane. Since the trajectory of the low P_t track is not a perfect circle due to energy loss, hit wires included in the circle are divided into two groups, one for a positive track and the other for a negative track as shown in Figure 3.7. The number of the wires in the group must be greater than or equal to three, otherwise the circle cannot be calculated. Although the momentum of the true track is expected to be greater than that of the false track, the resolution is not good enough to distinguish the two.

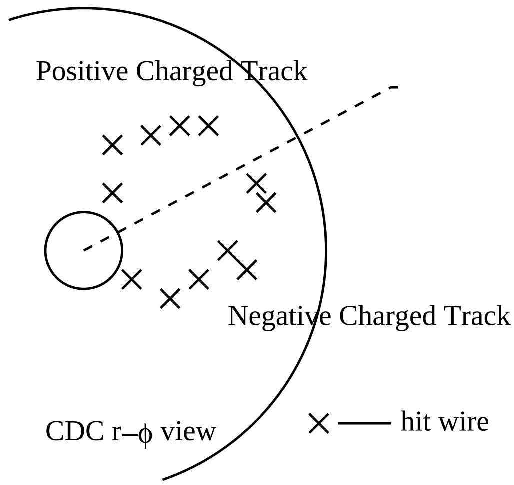

Figure 3.7: Positive and negative charged tracks in the r–ϕ plane. The direction of the magnetic field runs upward.

At the final stage of the curl finder, the circle is refitted using drift distance to improve the track parameters. If the distance between "a wire + its drift distance" and the circle is greater than 4.5cm, the wire is removed from the circle. The cut value is loose since the resolution of the track parameters themselves may not be good enough. After all bad hits are removed, the circle is recalculated again. If the distance is greater than 1.5cm, the wire is removed from the circle.

3.3 Stereo Finder for Curl Tracks

Tracks found by the curl finder in r–ϕ plane are reconstructed in the three dimensional space using "stereo finder". The stereo finder associates stereo hit wires with the tracks in the r–ϕ plane. A cylinder on which the track trajectory exists is expanded into a plane in the stereo finder as shown in Figure 3.8. Stereo hit wires are selected and checked in this plane. A horizontal axis is called "arc" ($= r \times \phi$) and a vertical axis corresponds to the z-coordinate. And then, track parameters are obtained by three dimensional fit using selected axial and stereo hit wires. In this fit, a track trajectory is treated as a spiral although it is not exactly correct due to the energy loss and the multiple scattering. The Kalman filtering technique is applied later to take into account those effect and obtain correct tracking parameters.

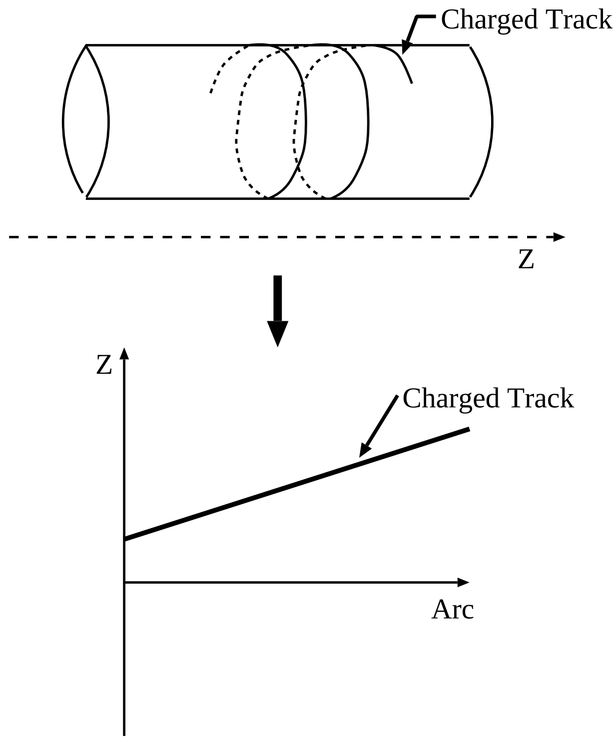

Figure 3.8: Expansion of the cylinder into a plane. A horizontal axis is called "arc" and a vertical axis corresponds to the z-coordinate.

As described above, the stereo finder associates stereo hit wires to the r–ϕ tracks in the r–ϕ plane first. When a stereo wire is projected into the r–ϕ plane, it becomes a line with a length of about 12cm. If a distance between r–ϕ position of the stereo wire at $z = 0$ and the circle is less than $5 \sim 9$cm, the stereo wire is included in the track. The exact cut value depends on the super layer since the wire length is different among them. Since we have two track candidates, positive and negative tracks, from one circle, stereo hit wires are shared by those two candidates. Stereo wires in the "right" side are associated with the tracks. Figure 3.9 illustrates the "right" and "wrong" side for positive and negative tracks. The r–ϕ position at $z = 0$ for each stereo wire is shown by the cross mark in the figure.

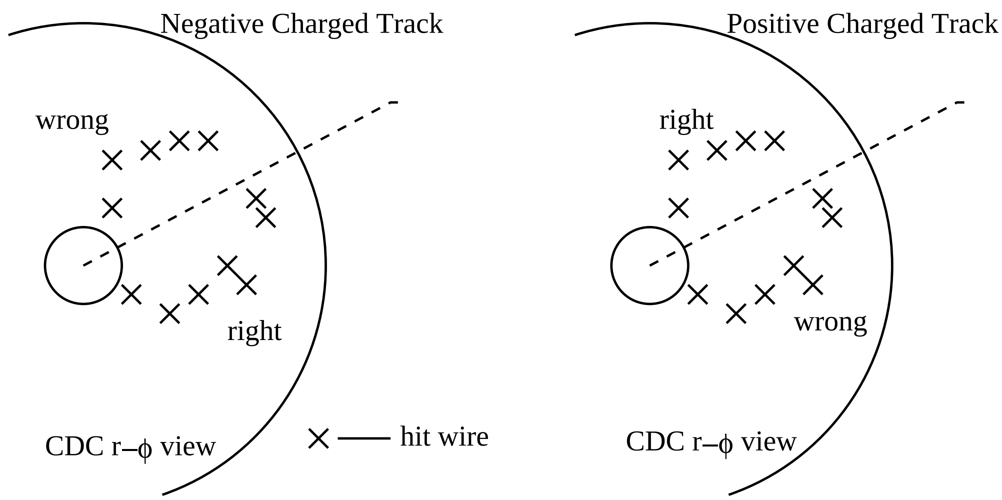

Figure 3.9: “Right” and “wrong” side of stereo wires. The cross mark indicates the r–ϕ position at $z = 0$ for each stereo wire.

After stereo hit wires are associated with the circle, “arc” and z position of each stereo wire are calculated. The arc and z pairs are obtained at the position where the drift circle of the stereo hit and the track circle touches. Generally, we have two solutions as illustrated in Figure 3.10. Sometimes, we have three or four solutions as shown in Figure 3.11. The wire with more than two solutions is not used since it is difficult to select the right solution in the fit. It does not caused a problem since it rarely happens.

When we have two consecutive hit wires in one layer, z positions of the hits are expected to be close to each other. One pair of (arc, z) with the minimum z difference is selected among four possible pairs. If the minimum z difference is greater than 10cm, the hits are considered bad and ignored afterward.

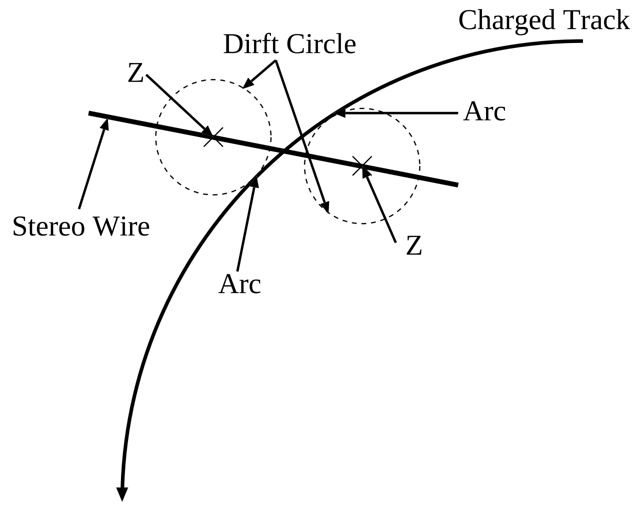

Figure 3.10: Determination of “arc” and z position of stereo wires.

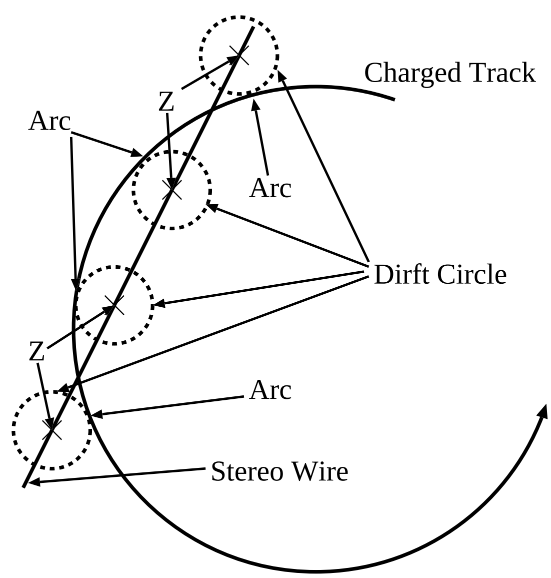

Figure 3.11: Determination of “arc” and z position of stereo wires with 4 solutions.

When we have three consecutive stereo hit wires in one layer, the best combination of (arc, z) pairs is selected based on z-differences. In each combination, we have three z-differences. The smallest of the three is called $d\mathrm{Z}_1$ and the second smallest is called $d\mathrm{Z}_2$. Figure 3.12 illustrates the definition of the $d\mathrm{Z}_1$ and $d\mathrm{Z}_2$. A combination with minimum $d\mathrm{Z}_1$ and $d\mathrm{Z}_2$ is selected. When $d\mathrm{Z}_2$ is less than 20cm, the minZ, which is a new parameter to use in the case of the greater than three consecutive wires, is defined as $d\mathrm{Z}_2 \div 2$ and three hits are considered to be good. When $d\mathrm{Z}_2$ is greater than 20cm and $d\mathrm{Z}_1$ is less than 10cm, two wires which give the $d\mathrm{Z}_1$ are considered to be good. The other wire is flagged as bad and ignored afterward. The minZ is defined as $d\mathrm{Z}_1$. Any combination which does not satisfy either condition is considered bad and the minZ is not defined.

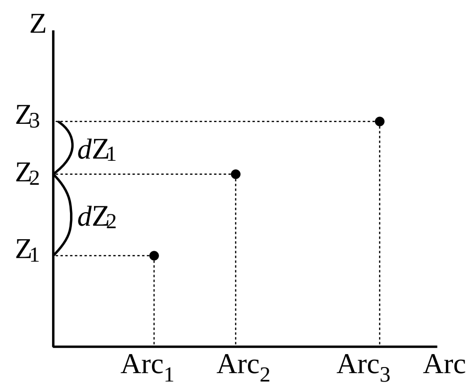

Figure 3.12: Definition of $d\mathrm{Z}_1$ and $d\mathrm{Z}_2$.

When we have four or more consecutive stereo hit wires in one layer, the best three consecutive wire combination is selected using the minZ. The other wires are flagged as unused and ignored afterward. Figure 3.13 illustrates three possible combinations of three consecutive wire hits when we have five consecutive wire hits in one layer.

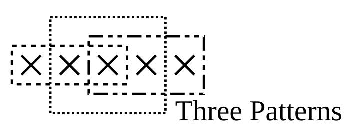

Figure 3.13: Five Consecutive Wires → Three Combinations of Three Consecutive Wires

When we have only one hit wire (isolated wire) in one layer, unique solution for (arc,z) pair can not be obtained. Such hit wires are put aside until the line is found using the wires above.

After (arc, z) pairs are calculated for all good stereo hits in each super layer, bad hits are removed further as follows.

Hits close to each other are associated to remove bad hits. The association starts from the hits in the innermost layer for each super layer. Wires in the second layer are selected when they are within "two distance" from the wires in the innermost layer as shown in Figure 3.14.

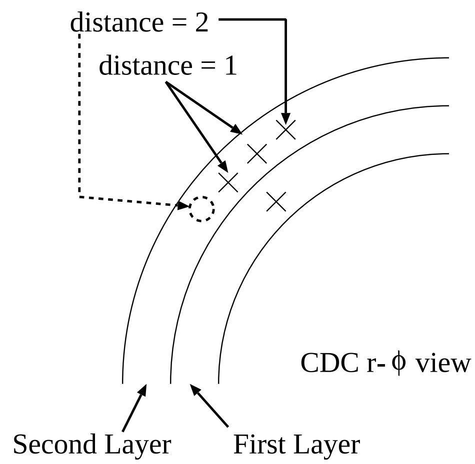

Figure 3.14: Association of wires between the first and second layers.

Wires in the third layer are associated with the wires in the second layer in the same manner as above. When there is no associated wire in the second layer, wires are associated with the wire in the first layer, as shown in Figure 3.15.

Wires in the subsequent layers are associated in the same manner as above.

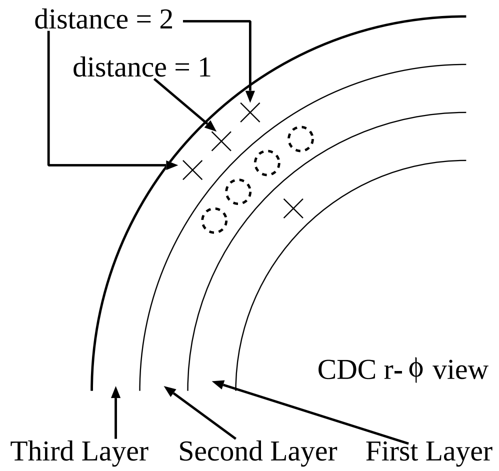

Figure 3.15: Association of wires between the first and third layers.

Hits are also removed from the selected hits if the z value are apart from the line defined by hits with minimum and maximum arc value. Figure 3.16 illustrates the case one hit is apart from the line.

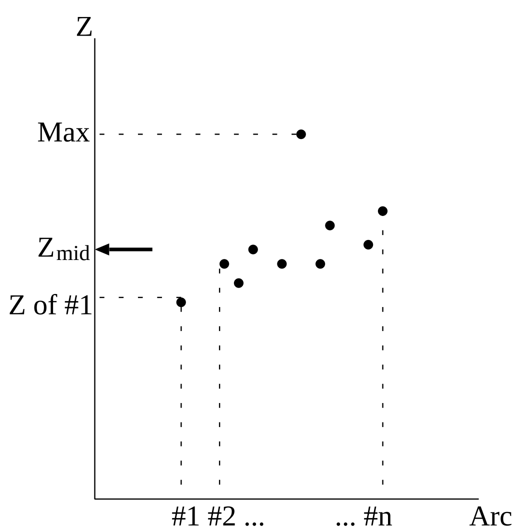

Figure 3.16: Validity of the maximum or minimum z wire

A value F is calculated for hits with the maximum or minimum z value (hits with maximum and minimum arc value is excluded) to evaluate the distance as,

$$\begin{aligned} Z_{mid} &\equiv (Z_1 + Z_n) \div 2 \\ F &\equiv \left| \frac{Z_{max}(Z_{min}) - Z_{mid}}{Z_1 - Z_{mid}} \right| . \end{aligned}$$

If F is greater than 2.5, the hit with $Z_{max}(Z_{min})$ is removed.

A line is obtained in the arc-z plane by using the selected wires. At this stage, hit wires, which are isolated in one layer, are considered. If the distance between the hit wire and the line in the arc-z plane is less than 5cm, the (arc, z) pair is appended to the line.

After all of the procedures described above are performed in each super layer, the line is refitted combining all remaining wires as shown in Figure 3.17.

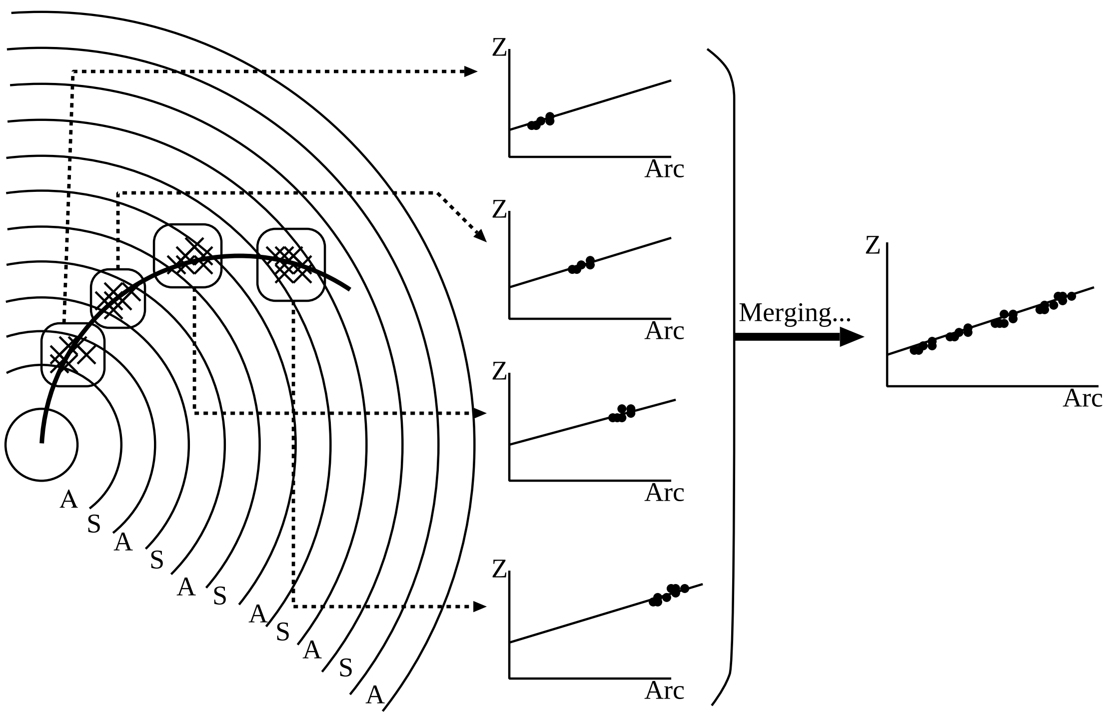

Figure 3.17: Merge Lines

The χ^2 per degree of freedom of the new line must be less than 25, and the difference of the slope from the original slope in each super layer must be less 10% of the original slope. If both conditions are not satisfied, combination of the super layers which satisfy both conditions are searched. When there are more than one combinations, the combination which includes more inner super layers is used since inner super layers are more important for low P_t tracks. When no good combination is found, the super layer with better χ^2 per degree of freedom is used within the first or the second super layer.

All of individual stereo wires are examined to find any wires removed by mistake. If the distance between the hit wire and the line in the arc-z plane is less than 1.5cm, the (arc, z) pair is appended to the new line. Finally, the stereo hit wires found above are used to reconstruct a track trajectory in three dimensional space. The reconstruction algorithm is described in Appendix B.

3.4 Performance

Performance of the low P_t reconstruction program is examined using 10^4 Monte Carlo events. Single pion is generated and detector response is simulated using GEANT3[12] simulation library developed at CERN[1]. In this study, some effects such as energy loss, multiple scattering and decays in flight are not simulated. The conformal finder is not used in order to check the performance of the curl finder. Figure 3.18 shows relations between reconstructed momentum and generated momentum. Figure 3.19 shows transverse momentum. There is not systematic deviation from the generated momentum.

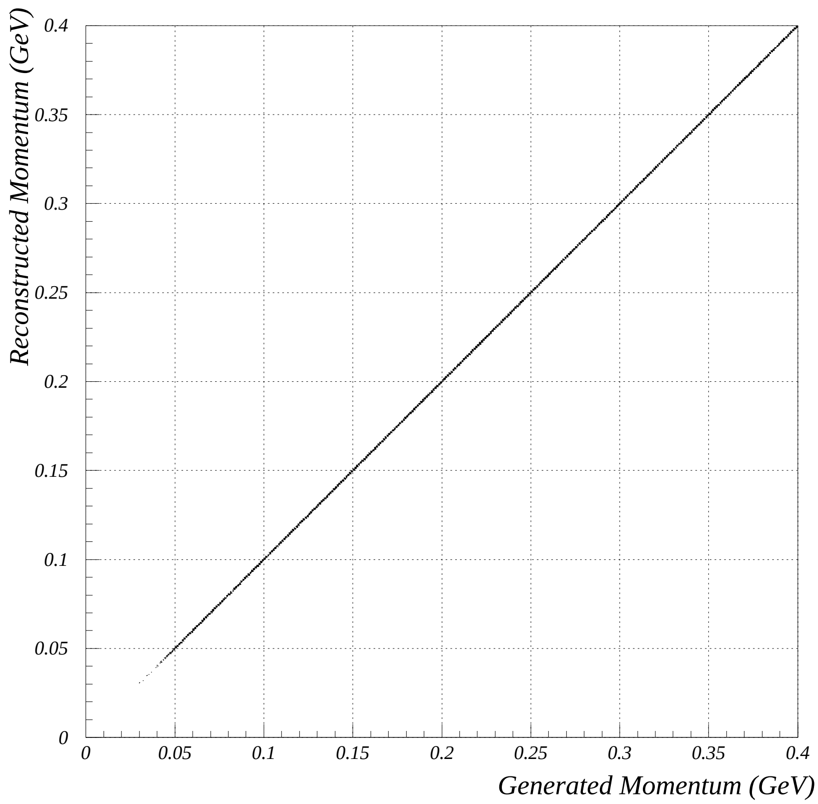

Figure 3.18: Generated Momentum .vs. Reconstructed Momentum

[1] Appendix C

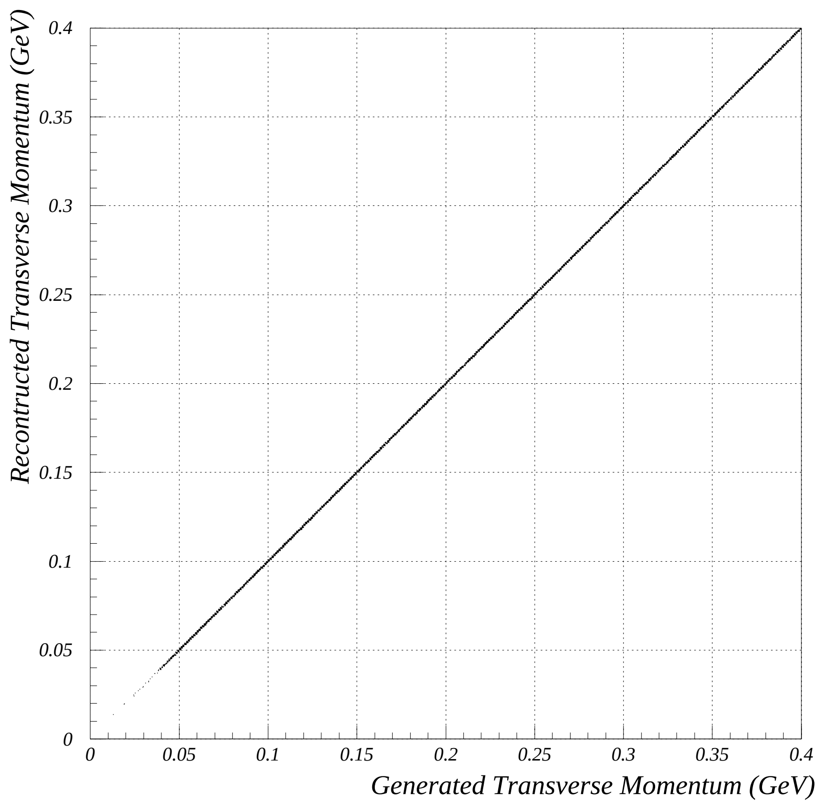

Figure 3.19: Generated Transverse Momentum .vs. Reconstructed Transverse Momentum

Figure 3.20 shows the efficiency as a function of the P_t for the same Monte Carlo simulation conditions. The solid and dashed line indicates the efficiencies with and without the low P_t track reconstruction program. The great improvement can be seen in the range, $P_t = 50\mathrm{MeV}/c \sim 120\mathrm{MeV}/c$. The efficiencies are not improved in the range, $P_t > 200\mathrm{MeV}/c$. It is reasonable because the radius of the outer of the CDC is 88cm(Chapter 2) and $P_t \sim 300 \times 1.5$(Tesla) $\times\ 0.88/2$(m) $\sim 200\mathrm{MeV}/c$.

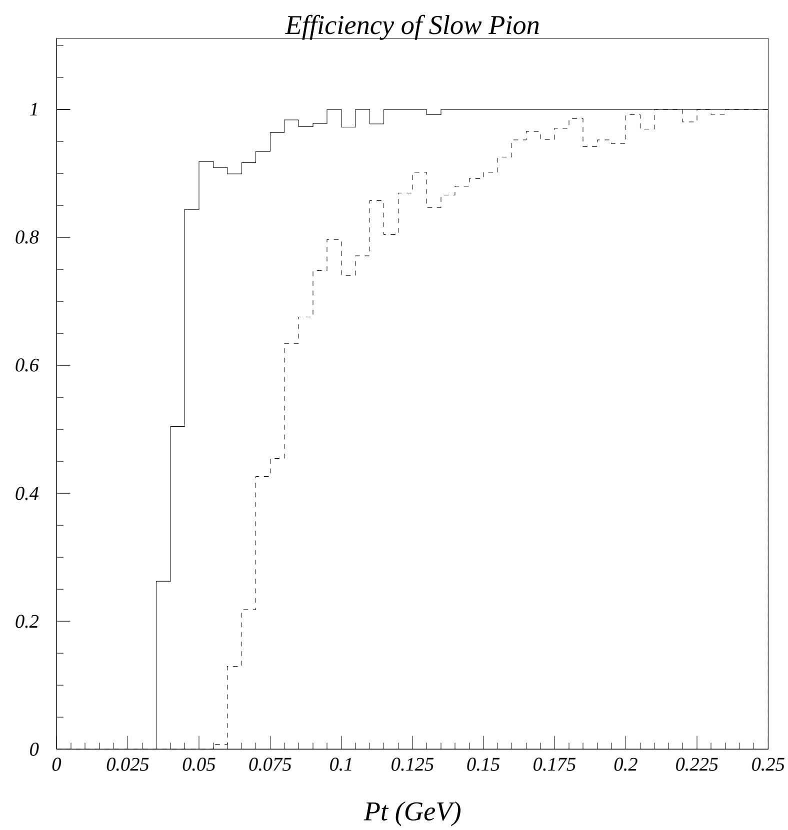

Figure 3.20: Track finding efficiency as a function of P_t for single pion events. The solid and dashed line indicates the efficiencies with and without the low P_t track reconstruction program, respectively.

Events with $\Upsilon(4S) \rightarrow B^0\overline{B^0}$, $B^0 \rightarrow D^{*-}e^+\nu_e$, $\overline{B^0} \rightarrow$ Generic Decay are also generated to measure the performance in more realistic condition by the full simulator(GSIM). In the simulation, the SVD information is used for calculation of the momentum. All charged particles are considered as pion and kaon. D^{*-} reconstruction efficiency is measured to be 22% without the low P_t reconstruction program, and it is improved to be 30% with the low P_t reconstruction program. Figure 3.21 shows the D^{*-}–$\overline{D^0}$ mass distributions with and without the low P_t reconstruction program. It is clear that the number of reconstructed D^{*-} increases by the low P_t reconstruction program. Tracking efficiencies are also measured as shown in Figure 3.22. The result is worse than that with single pion events due overlaps of tracks. Further optimization of bad hit rejections are required to improve the efficiency.

Figure 3.23 shows a multiplicity of the relation between generated tracks and reconstructed tracks. Track reconstruction programs make slightly more tracks than number of generated tracks.

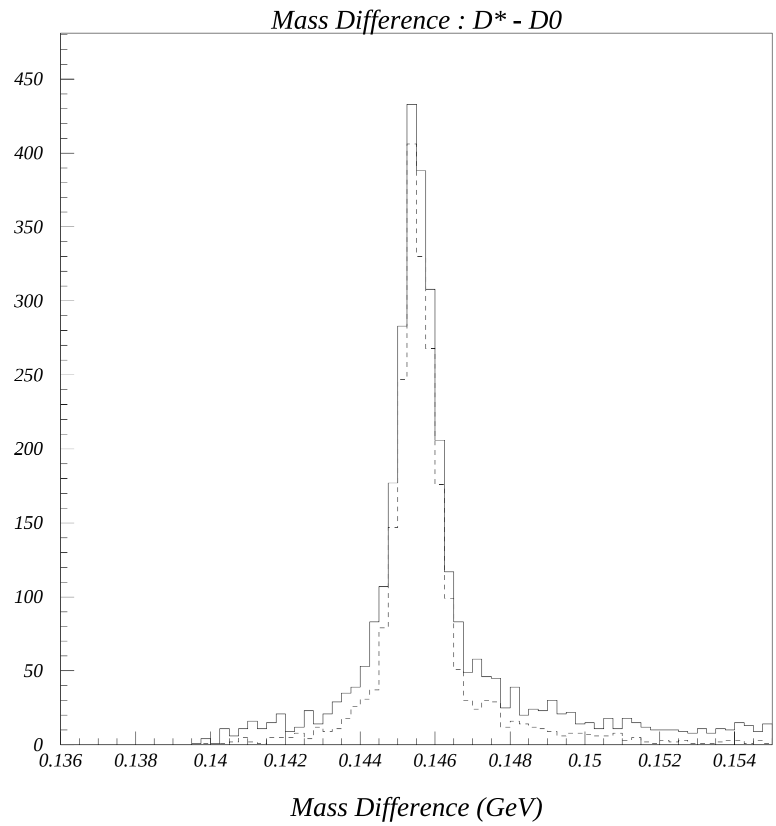

Figure 3.21: Mass difference between D^{*-} - $\overline{D^0}$. The solid and dashed line indicates the distributions with and without the low P_t track reconstruction program, respectively.

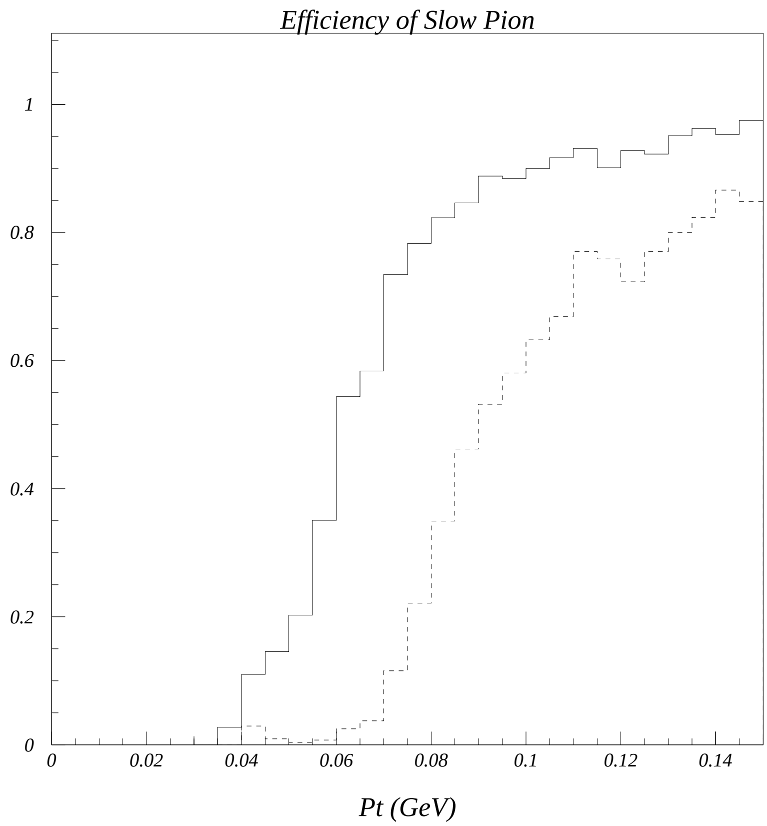

Figure 3.22: Track finding efficiency as a function of P_t. The solid and dashed line indicates the efficiencies with and without the low P_t track reconstruction program, respectively.

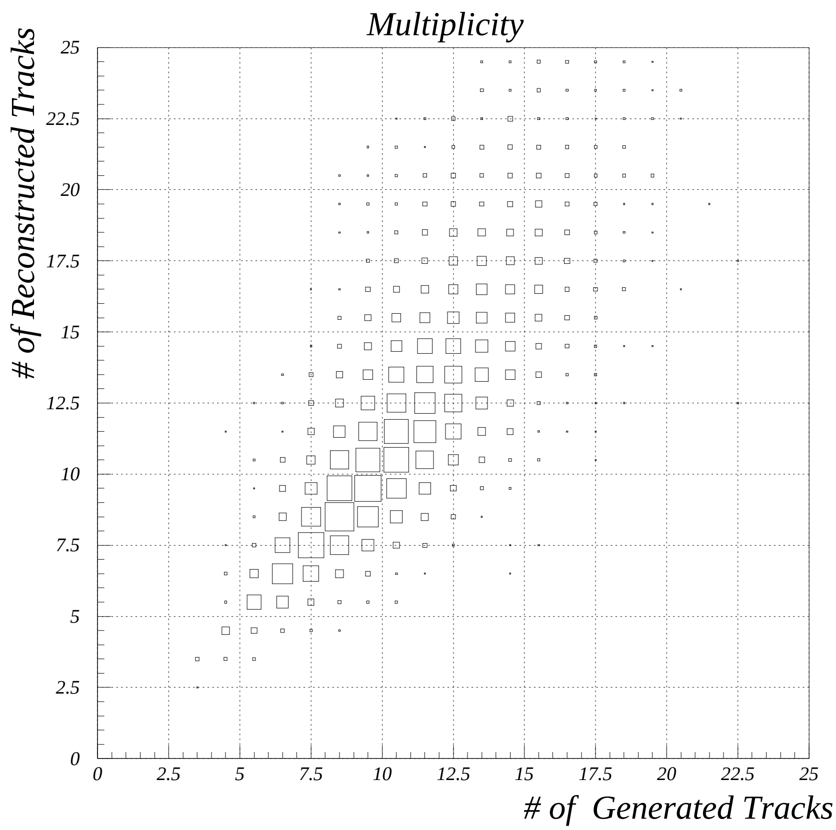

Figure 3.23: Multiplicity of Generated Tracks .vs. Reconstructed Tracks

Chapter 4

Development of The Kinematic Fitter

4.1 Introduction

Kinematic Fitter[6][7] is fitting programs with which values such as momentum of the reconstructed particle are improved using physics constraints in the process of reconstructing particle from its daughter particles.

Using these fitters in the physics analysis, vertices can be found and values of 4-momentum etc. can be improved. If one particle is reconstructed from wrong daughter particles using these fitters, χ^2 is large, that is, CL is near 0. Therefore, S/N ratio can be improved by CL cut in the analysis.

I have developed three type fitters as follows.

1. Assumption that the daughter particles should pass through a common decay vertex. (Figure 4.1)

   $\Longrightarrow$ Vertex Fitter

2. Assumption that reconstructed mass using the daughter particles is equal to an invariant mass. (Figures 4.2 and 4.3)

   $\Longrightarrow$ Mass Constraint Fitter

3. 1 and 2 simultaneously.

   $\Longrightarrow$ Vertex and Mass Constraint Fitter

The vertex fitter and mass constraint fitter are described in Reference [6]. I implemented them[7] in BELLE softwares. All programs are developed using C++ programming language [1].

[1] Sample programs[6] are written in Fortran.

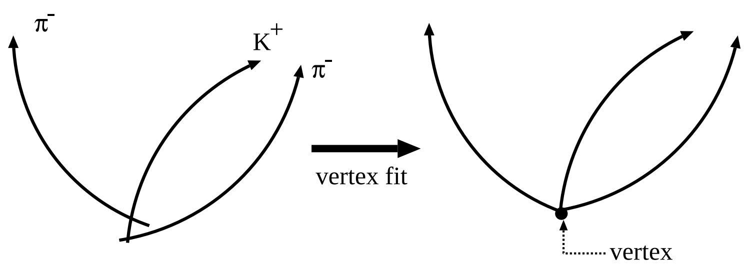

Figure 4.1: Vertex Fit

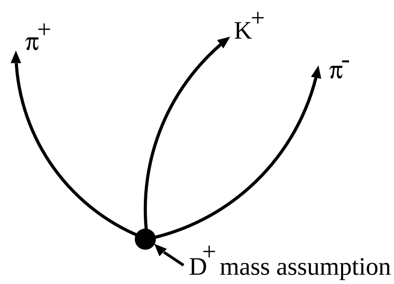

Figure 4.2: Mass Constraint Fit

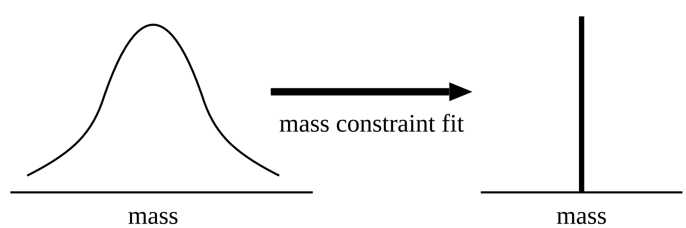

Figure 4.3: Mass Constraint Fit. A mass distribution becomes like a delta function using the mass constraint fit.

4.2 Algorithm

4.2.1 Overview

The method of the fit is the least square method of χ^2[6]. Terms for giving constraints are added to the χ^2 by the Lagrange multipliers. Generally, it is necessary to iterate by the Newton method to obtain the least χ^2. However, the least χ^2 can be obtained analytically by the linearlization of the constraint equations. It can save CPU time.

4.2.2 Fitting with Constraints

$\boldsymbol{\alpha}$ which has n components is a vector as follows.

$$\boldsymbol{\alpha} = \begin{pmatrix} \alpha_1 \\ \alpha_2 \\ \vdots \\ \alpha_n \end{pmatrix}$$

Initially the track parameters have the unconstrained values $\boldsymbol{\alpha}_0$(for example, measurement values). The r functions describing the constraints can be written generally as $\boldsymbol{H}(\boldsymbol{\alpha}) = 0$ as follows.

$$\boldsymbol{H} = \begin{pmatrix} H_1 \\ H_2 \\ \vdots \\ H_r \end{pmatrix}$$

Expanding around a convenient point $\boldsymbol{\alpha}_A$ yields the linearized equations,

$$0 = \boldsymbol{H}(\boldsymbol{\alpha}_A) + \frac{\partial \boldsymbol{H}(\boldsymbol{\alpha}_A)}{\partial \boldsymbol{\alpha}}(\boldsymbol{\alpha} - \boldsymbol{\alpha}_A) \equiv \boldsymbol{d} + \boldsymbol{D}\delta\boldsymbol{\alpha}$$

where $D_{ij} = \partial H_i / \partial \alpha_j$, $\delta\boldsymbol{\alpha} = \boldsymbol{\alpha} - \boldsymbol{\alpha}_A$.

The constraints are incorporated using the method of Lagrange multipliers in which the χ^2 is written as a sum of two terms,

$$\begin{aligned} \chi^2 &= (\delta\boldsymbol{\alpha} - \delta\boldsymbol{\alpha}_0)^T \boldsymbol{V}_{\alpha_0}^{-1}(\delta\boldsymbol{\alpha} - \delta\boldsymbol{\alpha}_0) + 2\boldsymbol{\lambda}^T(\boldsymbol{D}\delta\boldsymbol{\alpha} + \boldsymbol{d}) \\ &= (\boldsymbol{\alpha} - \boldsymbol{\alpha}_0)^T \boldsymbol{V}_{\alpha_0}^{-1}(\boldsymbol{\alpha} - \boldsymbol{\alpha}_0) + 2\boldsymbol{\lambda}^T\{\boldsymbol{D}(\boldsymbol{\alpha} - \boldsymbol{\alpha}_A) + \boldsymbol{d}\} \\ \boldsymbol{V}_{\delta\alpha_0} &= \boldsymbol{V}_{\alpha_0} \end{aligned}$$

where $\boldsymbol{\lambda}$ is a vector of r unknown parameters.

Minimizing the χ^2 with respect to $\delta\boldsymbol{\alpha}$ and $\boldsymbol{\lambda}$ yields two vector equations which can be solved for $\boldsymbol{\alpha}$ and their covariance matrix. The solution is shown as follows,

$$\boldsymbol{\alpha} = \boldsymbol{\alpha}_0 - \boldsymbol{V}_{\alpha_0}\boldsymbol{D}^T\boldsymbol{\lambda}$$

$$
\begin{aligned}
(\delta\boldsymbol{\alpha} &= \delta\boldsymbol{\alpha}_0 - \boldsymbol{V}_{\alpha_0}\boldsymbol{D}^T\boldsymbol{\lambda}) \\
\boldsymbol{\lambda} &= \boldsymbol{V}_D(\boldsymbol{D}\delta\boldsymbol{\alpha}_0 + \boldsymbol{d}) \\
\boldsymbol{V}_D &= (\boldsymbol{D}\boldsymbol{V}_{\alpha_0}\boldsymbol{D}^T)^{-1} \\
\boldsymbol{V}_\alpha &= \boldsymbol{V}_{\alpha_0} - \boldsymbol{V}_{\alpha_0}\boldsymbol{D}^T\boldsymbol{V}_D\boldsymbol{D}\boldsymbol{V}_{\alpha_0} \\
\chi^2 &= \boldsymbol{\lambda}^T\boldsymbol{V}_D^{-1}\boldsymbol{\lambda} = \boldsymbol{\lambda}^T(\boldsymbol{D}\delta\boldsymbol{\alpha}_0 + \boldsymbol{d})
\end{aligned} \tag{4.1}
$$

where $\delta\boldsymbol{\alpha} = \boldsymbol{\alpha} - \boldsymbol{\alpha}_A, \delta\boldsymbol{\alpha}_0 = \boldsymbol{\alpha}_0 - \boldsymbol{\alpha}_A$. To obtain the solution, the property of the symmetric matrix is used. $\boldsymbol{V}_{\alpha_0}$ is a symmetric matrix, and $\boldsymbol{V}_D$ is a symmetric matrix because the inversion of the symmetric matrix is symmetric. $\boldsymbol{\alpha}$ satisfies the constraints and it can be shown the diagonal elements of the covariance matrix are smaller than before.

When constraints are applied, the effective number of unknowns, that is, the degree of freedom in the fit is reduced by the number of constraints. The χ^2 equation is written with n parameters with the r constraint equations. By substituting the r constraints in the χ^2 equation, one is left with an expression having $n - r$ unknowns.

4.2.3 Fitting with Constraints for Unknown Parameters

$\boldsymbol{\alpha} = (\alpha_1, \alpha_2, ..., \alpha_n)$ represents a set of tracks and $\boldsymbol{v} = (v_1, v_2, ..., v_q)$ represents unknown parameters. The r constraint equations $\boldsymbol{H}(\boldsymbol{\alpha}, \boldsymbol{v}) = 0$ can be expanding around $\boldsymbol{\alpha}_A, \boldsymbol{v}_A$ to give the linearized equations as follows.

$$
\begin{aligned}
\boldsymbol{H}(\boldsymbol{\alpha}_A, \boldsymbol{v}_A) + \frac{\partial \boldsymbol{H}(\boldsymbol{\alpha}_A, \boldsymbol{v})}{\partial \boldsymbol{\alpha}}(\boldsymbol{\alpha} - \boldsymbol{\alpha}_A) + \frac{\partial \boldsymbol{H}(\boldsymbol{\alpha}, \boldsymbol{v}_A)}{\partial \boldsymbol{v}}&(\boldsymbol{v} - \boldsymbol{v}_A) \\
&\equiv \boldsymbol{d} + \boldsymbol{D}\delta\boldsymbol{\alpha} + \boldsymbol{E}\delta\boldsymbol{v} \\
&= \sum_{j=1}^{n} D_{ij}\delta\alpha_j + \sum_{j=1}^{q} E_{ij}\delta v_j + d_i \ (i = 1...r) \\
&= 0
\end{aligned}
$$

where $\delta\boldsymbol{\alpha} = \boldsymbol{\alpha} - \boldsymbol{\alpha}_A, \delta\boldsymbol{v} = \boldsymbol{v} - \boldsymbol{v}_A, E_{ij} = \frac{\partial H(\alpha, v_A)_i}{\partial v_j}, D_{ij} = \frac{\partial H(\alpha_A, v)_i}{\partial \alpha_j}$. $\boldsymbol{E}$ is a $r \times q$ matrix, and $\boldsymbol{D}$ is a $r \times n$ matrix.

Large errors are assigned to the $\boldsymbol{v}$(covariance matrix $\boldsymbol{L}$). The linearized χ^2 is

$$
\begin{aligned}
\chi^2 &= (\delta\boldsymbol{\alpha} - \delta\boldsymbol{\alpha}_0)^T\boldsymbol{V}_{\delta\alpha_0}^{-1}(\delta\boldsymbol{\alpha} - \delta\boldsymbol{\alpha}_0) + (\delta\boldsymbol{v} - \delta\boldsymbol{v}_0)^T\boldsymbol{L}^{-1}(\delta\boldsymbol{v} - \delta\boldsymbol{v}_0) \\
&+ 2\boldsymbol{\lambda}^T(\boldsymbol{D}\delta\boldsymbol{\alpha} + \boldsymbol{E}\delta\boldsymbol{v} + \boldsymbol{d}) \\
&\equiv (\delta\tilde{\boldsymbol{\alpha}} - \delta\tilde{\boldsymbol{\alpha}}_0)^T\boldsymbol{V}_{\delta\tilde{\alpha}_0}^{-1}(\delta\tilde{\boldsymbol{\alpha}} - \delta\tilde{\boldsymbol{\alpha}}_0) + 2\boldsymbol{\lambda}^T(\tilde{\boldsymbol{D}}\delta\tilde{\boldsymbol{\alpha}} + \boldsymbol{d})
\end{aligned}
$$

where the quantities with ˜ over them have the $\boldsymbol{v}$ information appended to them. Thus

$$
\delta\tilde{\boldsymbol{\alpha}} = \begin{pmatrix} \delta\boldsymbol{\alpha} \\ \delta\boldsymbol{v} \end{pmatrix}, \tilde{\boldsymbol{D}} = \begin{pmatrix} \boldsymbol{D} & \boldsymbol{E} \end{pmatrix}, \boldsymbol{V}_{\delta\tilde{\alpha}_0} = \begin{pmatrix} \boldsymbol{V}_{\delta\alpha_0} & 0 \\ 0 & \boldsymbol{L} \end{pmatrix}.
$$

The solution which minimizes the χ^2 can be taken straightly from Equation (4.1).

$$\begin{aligned}
\delta\tilde{\boldsymbol{\alpha}} &= \delta\tilde{\boldsymbol{\alpha}}_0 - V_{\delta\tilde{\alpha}_0}\tilde{\boldsymbol{D}}^T\boldsymbol{\lambda} \\
\boldsymbol{\lambda} &= \boldsymbol{V}_{\tilde{D}}(\tilde{\boldsymbol{D}}\delta\tilde{\boldsymbol{\alpha}}_0 + \boldsymbol{d}) = \boldsymbol{V}_{\tilde{D}}(\boldsymbol{D}\delta\boldsymbol{\alpha}_0 + \boldsymbol{E}\delta\boldsymbol{v}_0 + \boldsymbol{d}) \\
\boldsymbol{V}_{\tilde{D}} &\equiv (\tilde{\boldsymbol{D}}\boldsymbol{V}_{\delta\tilde{\alpha}_0}\tilde{\boldsymbol{D}}^T)^{-1} = (\boldsymbol{D}\boldsymbol{V}_{\delta\alpha_0}\boldsymbol{D}^T + \boldsymbol{E}\boldsymbol{L}\boldsymbol{E}^T)^{-1} \\
\boldsymbol{V}_{\delta\tilde{\alpha}} &= \boldsymbol{V}_{\delta\tilde{\alpha}_0} - \boldsymbol{V}_{\tilde{\alpha}_0}\tilde{\boldsymbol{D}}^T\boldsymbol{V}_{\tilde{D}}\tilde{\boldsymbol{D}}\boldsymbol{V}_{\delta\tilde{\alpha}_0} \\
\chi^2 &= \boldsymbol{\lambda}^T\boldsymbol{V}_{\tilde{D}}^{-1}\boldsymbol{\lambda} = \boldsymbol{\lambda}^T(\tilde{\boldsymbol{D}}\delta\tilde{\boldsymbol{\alpha}}_0 + \boldsymbol{d}) \\
&= \boldsymbol{\lambda}^T(\boldsymbol{D}\delta\boldsymbol{\alpha}_0 + \boldsymbol{E}\delta\boldsymbol{v}_0 + \boldsymbol{d})
\end{aligned}$$

The expressions for $\boldsymbol{\alpha}, \boldsymbol{v}, \boldsymbol{V}_\alpha, cov(\boldsymbol{v}, \boldsymbol{\alpha})$ and $\boldsymbol{V}_v$ can be extracted from the full solution using

$$\delta\tilde{\boldsymbol{\alpha}} = \begin{pmatrix} \boldsymbol{\alpha} - \boldsymbol{\alpha}_A \\ \boldsymbol{v} - \boldsymbol{v}_A \end{pmatrix}, \boldsymbol{V}_{\delta\tilde{\alpha}} = \boldsymbol{V}_{\tilde{\alpha}} = \begin{pmatrix} \boldsymbol{V}_\alpha & cov(\boldsymbol{v}, \boldsymbol{\alpha}) \\ cov(\boldsymbol{\alpha}, \boldsymbol{v}) & \boldsymbol{V}_v \end{pmatrix}, \boldsymbol{V}_{\delta\tilde{\alpha}_0} = \boldsymbol{V}_{\tilde{\alpha}_0},$$

which gives

$$\begin{aligned}
\boldsymbol{\alpha} &= \boldsymbol{\alpha}_0 - \boldsymbol{V}_{\alpha_0}\boldsymbol{D}^T\boldsymbol{\lambda} \\
\boldsymbol{v} &= \boldsymbol{v}_0 - \boldsymbol{L}\boldsymbol{E}^T\boldsymbol{\lambda} \\
\boldsymbol{V}_\alpha &= \boldsymbol{V}_{\alpha_0} - \boldsymbol{V}_{\alpha_0}\boldsymbol{D}^T\boldsymbol{V}_{\tilde{D}}\boldsymbol{D}\boldsymbol{V}_{\alpha_0} \\
\boldsymbol{V}_v &= \boldsymbol{L} - \boldsymbol{L}\boldsymbol{E}^T\boldsymbol{V}_{\tilde{D}}\boldsymbol{E}\boldsymbol{L} = (\boldsymbol{V}_E^{-1} + \boldsymbol{L}^{-1})^{-1} \\
cov(\boldsymbol{v}, \boldsymbol{\alpha}) &= -\boldsymbol{L}\boldsymbol{E}^T\boldsymbol{V}_{\tilde{D}}\boldsymbol{D}\boldsymbol{V}_{\alpha_0}.
\end{aligned}$$

The auxiliary matrix$\boldsymbol{V}_{\tilde{D}}$ can be calculated using the Woodbury formula [2]

$$\begin{aligned}
\boldsymbol{V}_{\tilde{D}} &= \boldsymbol{V}_D - \boldsymbol{V}_D\boldsymbol{E}(\boldsymbol{V}_E^{-1} + \boldsymbol{L}^{-1})^{-1}\boldsymbol{E}^T\boldsymbol{V}_D \\
\boldsymbol{V}_D &\equiv (\boldsymbol{D}\boldsymbol{V}_{\alpha_0}\boldsymbol{D}^T)^{-1} \\
\boldsymbol{V}_E &\equiv (\boldsymbol{E}^T\boldsymbol{V}_D\boldsymbol{E})^{-1}.
\end{aligned}$$

And then in the second equation of $\boldsymbol{V}_v$, the Woodbury formula is used.

In the limit $\boldsymbol{L} \to \infty$, it is found that $\boldsymbol{V}_v \simeq \boldsymbol{V}_E$. Using this, $\boldsymbol{V}_{\tilde{D}}$ can be solved as follows.

$$\boldsymbol{V}_{\tilde{D}} \simeq \boldsymbol{V}_D - \boldsymbol{V}_D\boldsymbol{E}\boldsymbol{V}_v\boldsymbol{E}^T\boldsymbol{V}_D.$$

Next concerning λ, it is necessary to calculate the first term of $\boldsymbol{L}^{-1}$ because a sensible value can not be obtained. Using the Woodbury formula, the result becomes as follows.

$$\begin{aligned}
\boldsymbol{\lambda} &\simeq \boldsymbol{\lambda}_0 - \boldsymbol{V}_D\boldsymbol{E}\boldsymbol{V}_v\boldsymbol{E}^T\boldsymbol{\lambda}_0 \\
\boldsymbol{\lambda}_0 &\equiv \boldsymbol{V}_D(\boldsymbol{D}\delta\boldsymbol{\alpha}_0 + \boldsymbol{d}).
\end{aligned}$$

[2] This is $(\boldsymbol{A} + \boldsymbol{U}\boldsymbol{V}^T)^{-1} = \boldsymbol{A}^{-1} - \boldsymbol{A}^{-1}\boldsymbol{U}(1 + \boldsymbol{V}^T\boldsymbol{A}^{-1}\boldsymbol{U})^{-1}\boldsymbol{V}^T\boldsymbol{A}^{-1}$. This formula can be proved intuitively, that is, $(\boldsymbol{A} + \delta\boldsymbol{A})^{-1} = \boldsymbol{A}^{-1} - \boldsymbol{A}^{-1}\delta\boldsymbol{A}\boldsymbol{A}^{-1} + \boldsymbol{A}\delta\boldsymbol{A}\boldsymbol{A}^{-1}\delta\boldsymbol{A}\boldsymbol{A}^{-1} + ...$

And then, concerning $\boldsymbol{v}$,

$$\boldsymbol{v} \simeq \boldsymbol{v}_A - \boldsymbol{V}_E \boldsymbol{E}^T \boldsymbol{\lambda}_0.$$

At last χ^2 can be calculated as follows.

$$\chi^2 = \lambda_0^T(\boldsymbol{D}\delta\boldsymbol{\alpha}_0 + \boldsymbol{E}\delta\boldsymbol{v}_0 + \boldsymbol{d}).$$

The result is in the limit $\boldsymbol{L} \to \infty$ as follows.

$$\begin{aligned}
\boldsymbol{\alpha} &= \boldsymbol{\alpha}_0 - \boldsymbol{V}_{\alpha_0}\boldsymbol{D}^T\boldsymbol{\lambda} \\
\boldsymbol{v} &= \boldsymbol{v}_A - \boldsymbol{V}_E\boldsymbol{E}^T\boldsymbol{\lambda}_0 \\
\boldsymbol{V}_\alpha &= \boldsymbol{V}_{\alpha_0} - \boldsymbol{V}_{\alpha_0}\boldsymbol{D}^T\boldsymbol{V}_{\tilde{D}}\boldsymbol{D}\boldsymbol{V}_{\alpha_0} \\
\boldsymbol{V}_v &= \boldsymbol{V}_E \\
\boldsymbol{V}_{\tilde{D}} &= \boldsymbol{V}_D - \boldsymbol{V}_D\boldsymbol{E}\boldsymbol{V}_E\boldsymbol{E}^T\boldsymbol{V}_D \\
\boldsymbol{V}_D &\equiv (\boldsymbol{D}\boldsymbol{V}_{\alpha_0}\boldsymbol{D}^T)^{-1} \\
\boldsymbol{V}_E &\equiv (\boldsymbol{E}^T\boldsymbol{V}_D\boldsymbol{E})^{-1} \\
\boldsymbol{\lambda} &= \boldsymbol{\lambda}_0 - \boldsymbol{V}_D\boldsymbol{E}\boldsymbol{V}_E\boldsymbol{E}^T\boldsymbol{\lambda}_0 \\
\boldsymbol{\lambda}_0 &\equiv \boldsymbol{V}_D(\boldsymbol{D}\delta\boldsymbol{\alpha}_0 + \boldsymbol{d}) \\
\chi^2 &= \lambda_0^T(\boldsymbol{D}\delta\boldsymbol{\alpha}_0 + \boldsymbol{E}\delta\boldsymbol{v}_0 + \boldsymbol{d}) \\
cov(\boldsymbol{v}, \alpha) &= -\boldsymbol{V}_E\boldsymbol{E}^T\boldsymbol{V}_D\boldsymbol{D}\boldsymbol{V}_{\alpha_0} \\
\delta\boldsymbol{\alpha}_0 &= \boldsymbol{\alpha}_0 - \boldsymbol{\alpha}_A \\
\delta\boldsymbol{v}_0 &= \boldsymbol{v}_0 - \boldsymbol{v}_A
\end{aligned}$$

4.3 Application

I describe physics constraints and their representations, that is, their matrices for applying to the kinematic fitter.

In the representations below, $p_\perp$ is the momentum transverse to the magnetic field direction. B is the magnetic field strength whose unit is tesla. a is defined as $a = -cBQ \times 10^{-3}$ [3] where Q is the charge of the particle whose unit is the absolute value of the electron charge.

4.3.1 Vertex Fitter

The particle whose charge is Q is moving in a magnetic field of strength B. The trajectory of the particle is given by

$$\begin{aligned}
p_x &= p_{0x}\cos\frac{s_\perp}{\rho} + p_{0y}\sin\frac{s_\perp}{\rho} \\
p_y &= p_{0y}\cos\frac{s_\perp}{\rho} - p_{0x}\sin\frac{s_\perp}{\rho}
\end{aligned}$$

[3] c is defined from the velocity of photon. $c = 2.99792458$

$$
\begin{aligned}
p_z &= p_{0z} \\
E &= E_0 \\
x &= x_0 - \frac{p_{0x}}{a}\sin\frac{s_\perp}{\rho} - \frac{p_{0y}}{a}(1-\cos\frac{s_\perp}{\rho}) \\
y &= y_0 - \frac{p_{0y}}{a}\sin\frac{s_\perp}{\rho} + \frac{p_{0x}}{a}(1-cos\frac{s_\perp}{\rho}) \\
z &= z_0 + s_\perp \tan\lambda
\end{aligned}
$$

where (x_0, y_0, z_0) is one known position on the helix. $(p_{0x}, p_{0y}, p_{0z}, E_0)$ is its 4-momentum in the position, and $\rho = -p_t/a = p_t/(cBQ \times 10^{-3})$. They are functions of $s_\perp$. $s_\perp$ is the arc length in xy plane from (x_0, y_0, z_0) to (x, y, z).

The constraint equations are obtained by eliminating $s_\perp$ from these equations of motion. For each track i,

$$
H_{1i} \equiv p_{ix}\Delta y_i - p_{iy}\Delta x_i - \frac{a_i}{2}(\Delta x_i^2 + \Delta y_i^2) = 0 \tag{4.2}
$$

$$
H_{2i} \equiv \Delta z_i - \frac{p_{iz}}{a_i} sin^{-1}[a_i(p_{ix}\Delta x_i + p_{iy}\Delta y_i)/p_{\perp i}^2] = 0 \tag{4.3}
$$

where $\Delta x_i = v_x - x_i$ etc. $\boldsymbol{v} = (v_x, v_y, v_z)$ is a vertex point.

In case that the charge is zero,

$$
\begin{aligned}
H_{1i} &\equiv p_{ix}\Delta y_i - p_{iy}\Delta x_i = 0 \\
H_{2i} &\equiv \Delta z_i - \frac{p_{iz}}{p_{i\perp}^2}(p_{ix}\Delta x_i + p_{iy}\Delta y_i) = 0.
\end{aligned}
$$

From Equations (4.2), (4.3), $\boldsymbol{D}_i$, $\boldsymbol{E}_i$, and $\boldsymbol{d}_i$ can be calculated as follows.

$$
\boldsymbol{D} = \begin{pmatrix} \boldsymbol{D}_1 & & & & \boldsymbol{E}_1 \\ & \boldsymbol{D}_2 & & & \boldsymbol{E}_2 \\ & & \ddots & & \vdots \\ & & & \boldsymbol{D}_n & \boldsymbol{E}_n \end{pmatrix} \tag{4.4}
$$

$$
\boldsymbol{d} = \begin{pmatrix} \boldsymbol{d}_1 \\ \boldsymbol{d}_2 \\ \vdots \\ \boldsymbol{d}_n \end{pmatrix} \tag{4.5}
$$

$$
\begin{aligned}
\boldsymbol{D}_i &= \begin{pmatrix} \frac{\partial H_{1i}}{\partial p_{ix}} & \frac{\partial H_{1i}}{\partial p_{iy}} & \frac{\partial H_{1i}}{\partial p_{iz}} & \frac{\partial H_{1i}}{\partial x_i} & \frac{\partial H_{1i}}{\partial y_i} & \frac{\partial H_{1i}}{\partial z_i} \\ \frac{\partial H_{2i}}{\partial p_{ix}} & \frac{\partial H_{2i}}{\partial p_{iy}} & \frac{\partial H_{2i}}{\partial p_{iz}} & \frac{\partial H_{2i}}{\partial x_i} & \frac{\partial H_{2i}}{\partial y_i} & \frac{\partial H_{2i}}{\partial z_i} \end{pmatrix} \\
&= \begin{pmatrix} \Delta y_i & -\Delta x_i & 0 & p_{iy} + a_i\Delta x_i & -p_{ix} + a_i\Delta y_i & 0 \\ -p_{iz}S_iR_{ix} & -p_{iz}S_iR_{iy} & -\frac{sin^{-1}B_i}{a_i} & p_{ix}p_{iz}S_i & p_{iy}p_{iz}S_i & -1 \end{pmatrix} \\
\boldsymbol{E}_i &= \begin{pmatrix} \frac{\partial H_{1i}}{\partial v_x} & \frac{\partial H_{1i}}{\partial v_y} & \frac{\partial H_{1i}}{\partial v_z} \\ \frac{\partial H_{2i}}{\partial v_x} & \frac{\partial H_{2i}}{\partial v_y} & \frac{\partial H_{2i}}{\partial v_z} \end{pmatrix}
\end{aligned}
$$

$$
\begin{aligned}
&= \begin{pmatrix} -p_{iy} - a_i\Delta x_i & p_{ix} - a_i\Delta y_i & 0 \\ -p_{ix}p_{iz}S_i & -p_{iy}p_{iz}S_i & 1 \end{pmatrix} \\
\boldsymbol{d}_i &= \begin{pmatrix} H_{1i} \\ H_{2i} \end{pmatrix} \\
&= \begin{pmatrix} A_{1i} - \frac{1}{2}a_i(\Delta x_i^2 + \Delta y_i^2) \\ \Delta z_i - \frac{p_{iz}}{a_i} sin^{-1} B_i \end{pmatrix}
\end{aligned}
$$

Since an energy term generally is not independent, $\boldsymbol{\alpha}_i = (p_{ix}, p_{iy}, p_{iz}, x_i, y_i, z_i)$. S_i etc. are defined as follows[4].

$$
\begin{aligned}
A_1 &= \Delta y p_x - \Delta x p_y \\
A_2 &= \Delta x p_x + \Delta y p_y \\
B &= aA_2/p_\perp^2 \\
R_{x(y)} &= \Delta x(y) - 2p_{x(y)}A_2/p_\perp^2 \\
S &= \frac{1}{p_\perp^2\sqrt{1-B^2}}
\end{aligned}
$$

In case that the charge is zero, S_i etc. are redefined as follows.

$$
\begin{aligned}
a &= 0 \\
B &= 0 \\
R_{x(y)} &= \Delta x(y) - 2p_{x(y)}^2 \Delta x(y)/p_\perp^2
\end{aligned}
$$

4.3.2 Mass Constraint Fitter

The constraint equation is given by

$$
H \equiv (\sum E_i)^2 - (\sum p'_{ix})^2 - (\sum p'_{iy})^2 - (\sum p'_{iz})^2 - m_c^2 = 0 \tag{4.6}
$$

where p'_{ix} etc. are given as follows.

$$
\begin{aligned}
p'_x &= p_x - a\Delta y \\
p'_y &= p_y + a\Delta x \\
p'_z &= p_z \\
\Delta x &= x_c - x \\
\Delta y &= y_c - y
\end{aligned}
$$

The prime means that the momentum for the tracks is evaluated at the vertex point. (x_c, y_c, z_c) is a vertex point. And m_c is an invariant mass.

From Equation (4.6), $\boldsymbol{D}$ and $\boldsymbol{d}$ can be calculated as follows.

$$
\boldsymbol{D} = (\frac{\partial H}{\partial p_{1x}}, \frac{\partial H}{\partial p_{1y}}, \frac{\partial H}{\partial p_{1z}},
$$

[4] A suffix i is omitted

$$
\begin{aligned}
& \frac{\partial H}{\partial x_1},\ \frac{\partial H}{\partial y_1},\ \frac{\partial H}{\partial z_1},\cdots) \\
= \ & (-2p'_x + 2E\frac{p'_{1x}}{E_1},\ -2p'_y + 2E\frac{p'_{1y}}{E_1},\ -2p'_z + 2E\frac{p'_{1z}}{E_1}, \\
& 2a_1(p'_y - E\frac{p'_{1y}}{E_1}),\ -2a_1(p'_x - E\frac{p'_{1x}}{E_1}),\ 0,\cdots) \qquad (4.7)
\end{aligned}
$$

$$
\boldsymbol{d} \ = \ H \ = \ E^2 - p'^2_x - p'^2_y - p'^2_z - m_c^2 \qquad (4.8)
$$

where $E = \sum E_i, p'_x = \sum p'_{ix}$. As I mentioned above, an energy term generally is not independent in the calculation.

4.3.3 Vertex and Mass Constraint Fitter

The constraint equations are already given by Equations (4.2), (4.3), and (4.6). It is only to combine them for applying invariant mass fit and vertex fit simultaneously. To obtain $\boldsymbol{D}$, a matrix (4.7) and a new term E_{mass} for a vertex point are added in the last line of the matrix (4.4). And to obtain $\boldsymbol{d}$, a matrix (4.8) is added in the last line of the matrix (4.5). They are written as follows.

$$
\boldsymbol{D} = \begin{pmatrix} \boldsymbol{D}_1 & & & & \boldsymbol{E}_1 \\ & \boldsymbol{D}_2 & & & \boldsymbol{E}_2 \\ & & \ddots & & \vdots \\ & & & \boldsymbol{D}_n & \boldsymbol{E}_n \\ & \boldsymbol{D}_{\text{mass}} & & & \boldsymbol{E}_{\text{mass}} \end{pmatrix}, \boldsymbol{d} = \begin{pmatrix} \boldsymbol{d}_1 \\ \boldsymbol{d}_2 \\ \vdots \\ \boldsymbol{d}_n \\ \boldsymbol{d}_{\text{mass}} \end{pmatrix}
$$

$$
\boldsymbol{D}_i = \begin{pmatrix} \Delta y_i & -\Delta x_i & 0 & p_{iy} + a_i\Delta x_i & -p_{ix} + a_i\Delta y_i & 0 \\ -p_{iz}S_iR_{ix} & -p_{iz}S_iR_{iy} & -\frac{sin^{-1}B_i}{a_i} & p_{ix}p_{iz}S_i & p_{iy}p_{iz}S_i & -1 \end{pmatrix}
$$

$$
\boldsymbol{E}_i = \begin{pmatrix} -p_{iy} - a_i\Delta x_i & p_{ix} - a_i\Delta y_i & 0 \\ -p_{ix}p_{iz}S_i & -p_{iy}p_{iz}S_i & 1 \end{pmatrix}
$$

$$
\boldsymbol{d}_i = \begin{pmatrix} A_{1i} - \frac{1}{2}a_i(\Delta x_i^2 + \Delta y_i^2) \\ \Delta z_i - \frac{p_{iz}}{a_i}sin^{-1}B_i \end{pmatrix}
$$

$$
\begin{aligned}
\boldsymbol{D}_{\text{mass}} = \ & (-2p'_x + 2E\frac{p'_{1x}}{E_1},\ -2p'_y + 2E\frac{p'_{1y}}{E_1},\ -2p'_z + 2E\frac{p'_{1z}}{E_1}, \\
& 2a_1(p'_y - E\frac{p'_{1y}}{E_1}),\ -2a_1(p'_x - E\frac{p'_{1x}}{E_1}),\ 0,\cdots)
\end{aligned}
$$

$$
\boldsymbol{E}_{\text{mass}} = \left(2E\sum_i \frac{p'_{iy}a_i}{E_i} - 2p'_y\sum_i a_i, -2E\sum_i \frac{p'_{ix}a_i}{E_i} + 2p'_x\sum_i a_i, 0\right)
$$

$$
\boldsymbol{d}_{\text{mass}} = E^2 - p'^2_x - p'^2_y - p'^2_z - m_c^2
$$

where $E = \sum E_i,\ p'_x = \sum p'_{ix}$ and S, etc. are defined as the previous.

4.4 Performance

Benefits of the kinematic fitter are as follows.

- Improvement of the momentum.
- Calculation of the vertex position.
- Background rejection using confidence level cuts.

Following decay chain has been studied to demonstrate these abilities using 10^7 Monte Carlo events by the fast simulator(FSIM)[5].

$$
\begin{aligned}
B^0 &\rightarrow D^-\pi^+\pi^+\pi^- && (4.9)\\
D^- &\rightarrow K^+\pi^-\pi^- && (4.10)
\end{aligned}
$$

It is analyzed by two methods as follows.

1. mass cut, and beam energy constraint of B^0.
2. mass cut, beam energy constraint of B^0, and CL(confidence level) cut using the kinematic fitter. Mass Vertex Fitter for (4.10) and Vertex Fitter for (4.9) are used.

Analysis conditions are as follows.

- In the particle identification of kaon and pion [6], if a probability of kaon is greater than $1.5 \times$ probability of pion, a particle is considered as kaon. If not, it is as pion.
- If CL is greater than 2% and reconstructed mass is within 3σ mass cuts($=$ 4.2MeV $\times$ 3) from nominal mass, it is used in reconstructions.

Figure 4.4 compares momentum resolutions without and with the kinematic fitter. Plots in the left and right sides correspond to ΔP resolution without and with the kinematic fitter for x-component(upper), y-component(middle), z-component(bottom), respectively.

[5] Appendix C
[6] The way to determine probabilities is described in [11]

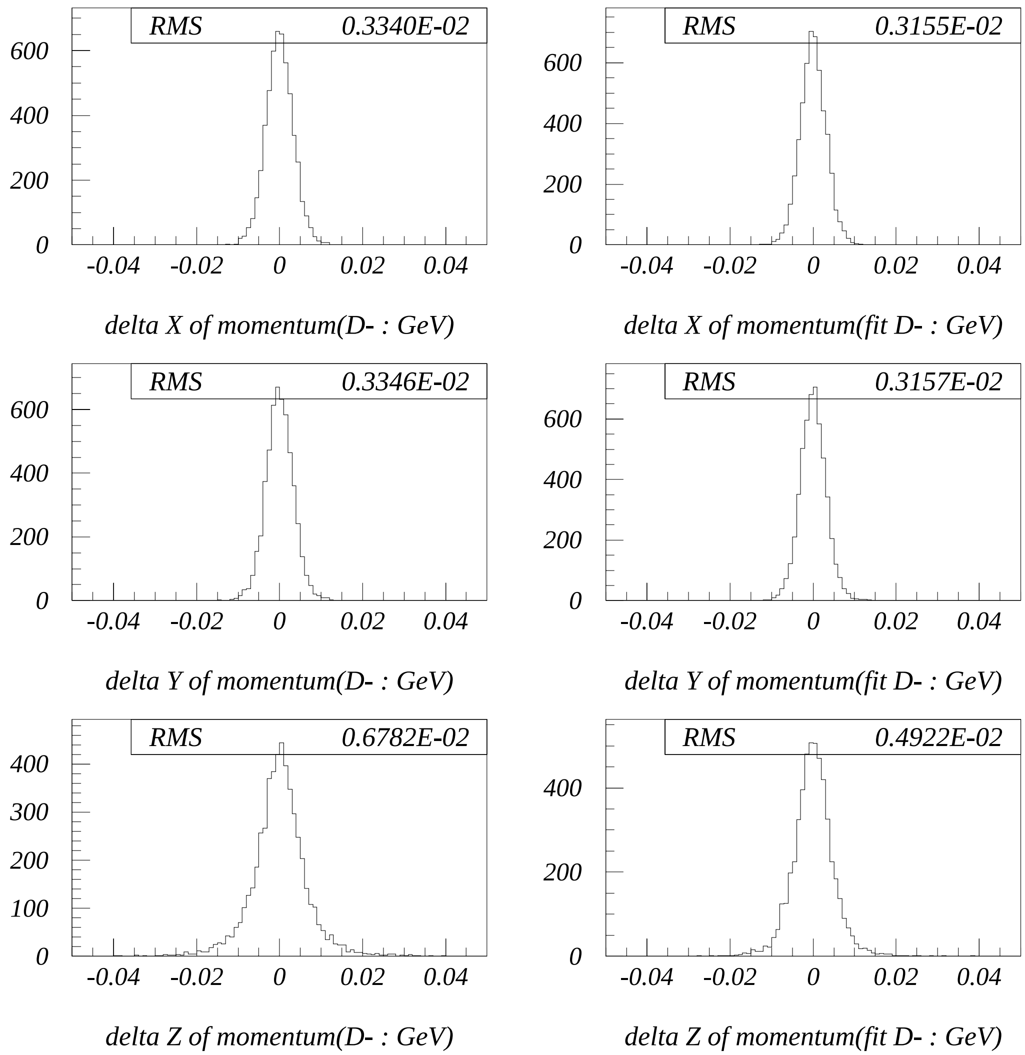

Figure 4.4: ΔMomentum of Vertex and Mass Constraint Fit to D^-: The left side is without kinematic fitters and the right side is with kinematic fitters.

ΔP_i is defined as ΔP_i = reconstructed $P_i - P_i$ of MC. P_i is a component $i (= x, y, z)$ of momentum.

Z component of momentum shows significant improvement (from $\sigma = 6.8$ MeV to 4.9 MeV).

Figure 4.5 shows Δz distribution of the vertex position obtained by the kinematic fitter. z is a component of vertex and is parallel with the beam pipe.

Δz is defined as,

$$\Delta z \quad = \quad z \text{ value from kinematic fitter} - z \text{ value from MC.}$$

The resolution is estimated to be $27 \mu m$ which is reasonably good.

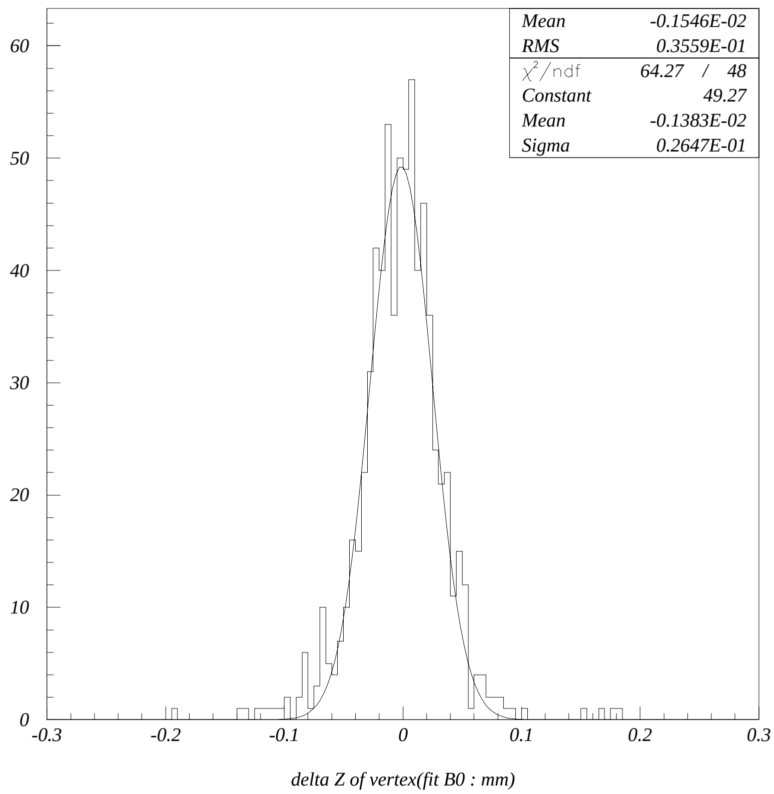

Figure 4.5: Δz of B^0 Vertex

Figure 4.6 compares confidence level(CL) distribution between signal and background. Solid histogram indicates a sum of signal and background and hatched histogram indicates signal. The signal distribution is flat while the background distribution peaks at CL=0 as expected.

When the candidates with CL>2% are selected, 35% of background are rejected while 98% of signal are retained.

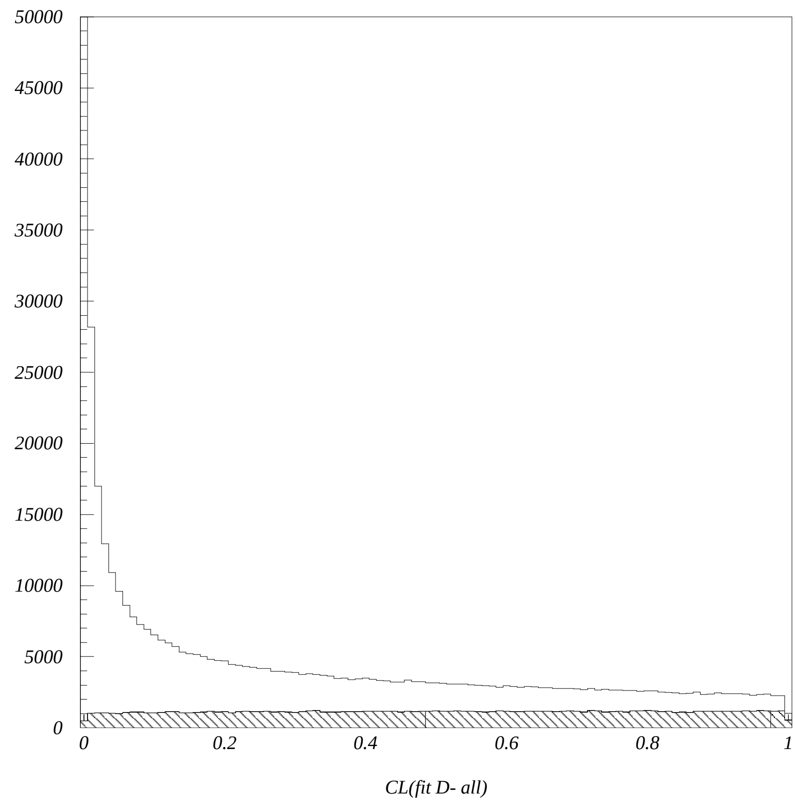

Figure 4.6: CL of Vertex and Mass Constraint Fit to D^-

Figures 4.7 and 4.8 show B^0 mass distributions without and with CL cuts, respectively. The solid histogram indicates a sum of signal and background and the hatched indicates background. Clearly, S/N ratio is improved after CL cuts and is calculated in 10^7 events as shown in Table 4.1 [7].

Method Number	Signal	Background	bb Background	Continuum Background	S/N
1	737	10846	4773	6073	0.068
2	710	4813	2285	2528	0.148

Table 4.1: S/N Ratio etc. of $B^0 \to D^-\pi^+\pi^+\pi^-$

[7] Background = $b\bar{b}$ Background + Continuum Background ($s\bar{s}$, $c\bar{c}$, $d\bar{d}$, $u\bar{u}$)

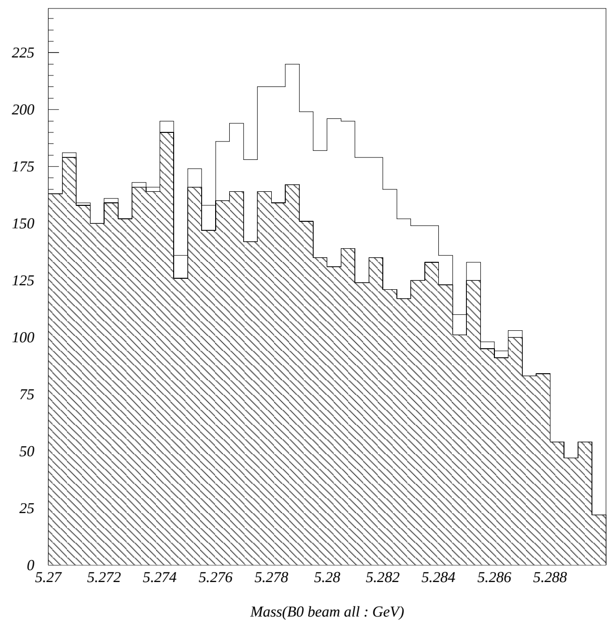

Figure 4.7: B^0 Mass Distribution without Kinematic Fitter

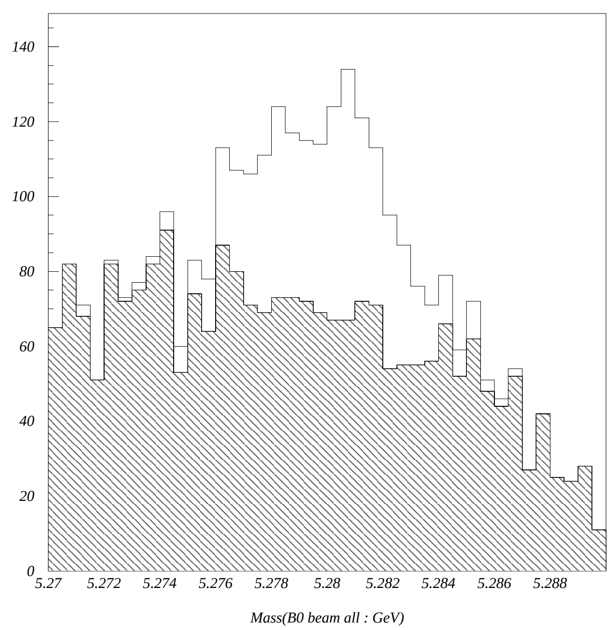

Figure 4.8: B^0 Mass Distribution with Kinematic Fitter

Chapter 5

Summary

Algorithm and procedure for a low momentum track reconstruction program and a kinematic fitter for the BELLE are described in detail.

Concerning the low momentum track reconstruction program, wire hit association and bad hit rejection procedures are described. In the performance check, track finding efficiencies are greatly improved in the region, $50 < P_t < 90$ MeV/c. D^{*-} reconstruction efficiency is found to improve by ~36%. This is very important for the measurement of the CP violation using $B^0 \to D^{*+}D^{*^-}$ decay since the efficiency improvement is squared. However further optimization of bad hit rejection is necessary to improve the efficiency. The SVD hit information may be used to improve the efficiency further when we do not have enough stereo hit wires.

Kinematic fitters can be used in the physics analysis. A fitter for finding vertices is crucial to measure CP violations because a determination of Δz is required. And a fitter for constraining an invariant mass is useful to improve reconstructed momentum as the resolution of z component of momentum is significantly improved from $\sigma = 6.8$MeV/c to 4.9 MeV/c. The confidence level of the kinematic fitter is useful to reject background events as S/N ratio is improved by a factor of 2.2 without loosing signal events.

Acknowledgments

Thanks are due to H. Aihara(Univ. of Tokyo), H. Tajima(Univ. of Tokyo) N. Katayama(KEK), T. Nozaki(KEK), H. Ozaki(KEK), S. Uno(KEK) Y. Iwasaki(KEK), Y. Ohnishi(KEK), and J. Suzuki(KEK) for their advice and suggestion.

Appendix A

Quantum mechanics of the neutral meson system

The flavor eigenstates, X^0 and $\bar{X}^0$, mix through the weak interactions as Figure A.1($B^0 - \overline{B^0}$) and form mass and life time eigenstates, X_+ and X_-. I describe how this mix is occurred by quantum mechanics.

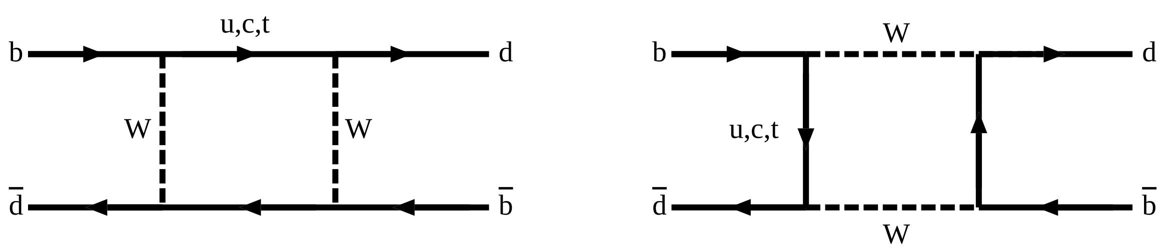

Figure A.1: Box Diagram of $B^0 - \overline{B^0}$ Mixing

Pseudo scalar neutral meson such as B^0, K^0 is written by X^0, and its CP transformation is defined as follows.

$$CP|X^0\rangle = -|\overline{X^0}\rangle \tag{A.1}$$

A state of the neutral meson at the time t is written by $|X(t)\rangle$, and it is expanded with $|X^0\rangle$ and $|\overline{X^0}\rangle$ as follows.

$$|X(t)\rangle \quad = \quad \alpha(t)|X^0\rangle + \beta(t)|\overline{X^0}\rangle$$

And its time evolution is described by the Schrödinger equation:

$$i\frac{d}{dt}|X(t)\rangle \quad = \quad H|X(t)\rangle,$$

that is,

$$i\frac{d}{dt}\begin{pmatrix}\alpha\\ \beta\end{pmatrix} = \begin{pmatrix}\langle X^0|H|X^0\rangle & \langle X^0|H|\overline{X^0}\rangle\\ \langle\overline{X^0}|H|X^0\rangle & \langle\overline{X^0}|H|\overline{X^0}\rangle\end{pmatrix}\begin{pmatrix}\alpha\\ \beta\end{pmatrix}. \qquad (A.2)$$

Because the neutral meson is not stable and decays to other particles and its wave function can be written as $e^{-i(E-i\gamma/2)t}$, Hamiltonian H can be defined using two hermite matrices, M and Γ :

$$\begin{aligned}\langle X^0|H|X^0\rangle &\equiv M_{11}-(i/2)\Gamma_{11},\ \ \langle X^0|H|\overline{X^0}\rangle \equiv M_{12}-(i/2)\Gamma_{12}\\ \langle\overline{X^0}|H|X^0\rangle &\equiv M_{12}^*-(i/2)\Gamma_{12}^*,\ \ \langle\overline{X^0}|H|\overline{X^0}\rangle \equiv M_{22}-(i/2)\Gamma_{22}.\end{aligned}$$

Assuming that mass and life time of particle are the same with these of its anti-particle using CPT invariance, the following equation is satisfied :

$$\langle X^0|H|X^0\rangle = \langle\overline{X^0}|H|\overline{X^0}\rangle \equiv M_0-(i/2)\Gamma_0.$$

Eigenvalues $\gamma_\pm$ and eigenvectors $|X_\pm\rangle$ of Equation (A.2) are,

$$\lambda_\pm = M_0-(i/2)\Gamma_0 \pm \sqrt{(M_{12}-(i/2)\Gamma_{12})(M_{12}^*-(i/2)\Gamma_{12}^*)} \qquad (A.3)$$

$$|X_\pm\rangle = \frac{p|X^0\rangle \pm q|\overline{X^0}\rangle}{\sqrt{|p|^2+|q|^2}}, \qquad (A.4)$$

where[1]

$$\frac{q}{p} = \frac{\sqrt{(M_{12}-(i/2)\Gamma_{12})(M_{12}^*-(i/2)\Gamma_{12}^*)}}{M_{12}-(i/2)\Gamma_{12}}. \qquad (A.5)$$

Let us define $M_\pm$ and $\Gamma_\pm$ as,

$$\lambda_\pm \equiv M_\pm-(i/2)\Gamma_\pm.$$

From them, the differences of the eigenstate mass and life time, respectively, ΔM and $\Delta\Gamma$ can be written :

$$\begin{aligned}\Delta M &= M_+-M_-\\ &= 2\mathrm{Re}\left(\sqrt{(M_{12}-(i/2)\Gamma_{12})(M_{12}^*-(i/2)\Gamma_{12}^*)}\right), \qquad (A.6)\\ \Delta\Gamma &= \Gamma_+-\Gamma_-\\ &= -4\mathrm{I}m\left(\sqrt{(M_{12}-(i/2)\Gamma_{12})(M_{12}^*-(i/2)\Gamma_{12}^*)}\right)\\ &= \frac{4}{\Delta M}\mathrm{R}e(M_{12}\Gamma_{12}^*). \qquad (A.7)\end{aligned}$$

From Equation (A.1), CP eigenstate can be written as,

$$|X_{even}\rangle = (|X^0\rangle - |\overline{X^0}\rangle)/\sqrt{2}, \quad |X_{odd}\rangle = (|X^0\rangle + |\overline{X^0}\rangle)/\sqrt{2}.$$

[1] Equation (A.3) is defined satisfying $\mathrm{Re}(\sqrt{(M_{12}-(i/2)\Gamma_{12})(M_{12}^*-(i/2)\Gamma_{12}^*)}) > 0$.

From them, states $|X_\pm\rangle$ are written as,

$$|X_\pm\rangle \quad = \quad \frac{1}{\sqrt{2(|p|^2+|q|^2)}}\{(p\mp q)|X_{even}\rangle + (p\pm q)|X_{odd}\rangle\}.$$

Let us consider the time evolution of the system which is $|X^0\rangle$ at $t = 0$. From Equation (A.4), $|X^0\rangle$ can be written as,

$$|X^0\rangle \quad = \quad \frac{\sqrt{|p|^2+|q|^2}}{2p}(|X_+\rangle + |X_-\rangle).$$

Similarly $|\overline{X^0}\rangle$ is written as,

$$|\overline{X^0}\rangle \quad = \quad \frac{\sqrt{|p|^2+|q|^2}}{2q}(|X_+\rangle - |X_-\rangle).$$

Since $|X_\pm\rangle$ evolutes following $e^{-i\lambda_\pm t}$,

$$\begin{aligned}
|X^0(t)\rangle &= \frac{\sqrt{|p|^2+|q|^2}}{2p}(e^{-i\lambda_+ t}|X_+\rangle + e^{-i\lambda_- t}|X_-\rangle) \\
&= \frac{e^{-i\lambda_+ t}}{2}\{g_+(t)|X^0\rangle + \frac{q}{p}g_-(t)|\overline{X^0}\rangle\}, && \text{(A.8)} \\
g_\pm(t) &= 1 \pm e^{i\{\Delta M-(i/2)\Delta\Gamma\}t}. && \text{(A.9)}
\end{aligned}$$

Similarly, the time evolution of the system which is $|\overline{X^0}\rangle$ at $t = 0$ is,

$$|\overline{X^0}(t)\rangle \quad = \quad \frac{e^{-i\lambda_+ t}}{2}\{\frac{p}{q}g_-(t)|X^0\rangle + g_+(t)|\overline{X^0}\rangle\} \qquad \text{(A.10)}$$

From Equations (A.8) and (A.10), the probability that the meson which is born at $t = 0$ as $X^0(\overline{X^0})$ is observed at $t = t$ as $\overline{X^0}(X^0)$ is,

$$\begin{aligned}
P(X^0 \to \overline{X^0};t) &= |\langle\overline{X^0}|X^0(t)\rangle|^2 = \frac{e^{-(\Gamma_0+\Delta\Gamma/2)t}}{4}\left|\frac{q}{p}\right|^2|g_-(t)|^2 \\
&= \frac{e^{-\Gamma_0 t}}{2}\left|\frac{q}{p}\right|^2\{\cosh(\Delta\Gamma t/2) - \cos(\Delta M t)\}, && \text{(A.11)} \\
P(\overline{X^0} \to X^0;t) &= |\langle X^0|\overline{X^0}(t)\rangle|^2 && \text{(A.12)} \\
&= \frac{e^{-\Gamma_0 t}}{2}\left|\frac{p}{q}\right|^2\{\cosh(\Delta\Gamma t/2) - \cos(\Delta M t)\} && \text{(A.13)}
\end{aligned}$$

And then, the decay rate of the meson which is $X^0(\overline{X^0})$ at $t = 0$ to a common CP eigenstate f_{CP} is,

$$\Gamma(X^0(t) \to f_{CP}) \quad = \quad \frac{e^{-(\Gamma_0+\Delta\Gamma/2)t}}{4}\Big|g_+(t)\langle f_{CP}|X^0\rangle$$

$$
\begin{aligned}
&& + \quad \frac{q}{p} g_-(t)\langle f_{CP}|\overline{X^0}\rangle \Bigg|^2, \quad \text{(A.14)} \\
\Gamma(\overline{X^0}(t) \to f_{CP}) &= \frac{e^{-(\Gamma_0+\Delta\Gamma/2)t}}{4} \Bigg| \frac{p}{q} g_-(t)\langle f_{CP}|X^0\rangle \\
&& + \quad g_+(t)\langle f_{CP}|\overline{X^0}\rangle \Bigg|^2. \quad \text{(A.15)}
\end{aligned}
$$

A.1 B meson : B^0

The assumption that $\Delta\Gamma/\Gamma \ll 1, |M_{12}| \gg |\Gamma_{12}|$ is reasonable. From this assumption and Equations (A.6), (A.7), (A.5),

$$
\begin{aligned}
\Delta M &\simeq 2|M_{12}|, \quad \Delta\Gamma \simeq 2|M_{12}|\mathrm{Re}\,(\Gamma_{12}/M_{12})\,, && \text{(A.16)} \\
|q/p|^2 &\simeq 1 - \mathrm{Im}\,(\Gamma_{12}/M_{12})\,. && \text{(A.17)}
\end{aligned}
$$

$B^0 - \overline{B^0}$ mixing

Equations (A.11) and (A.13) represent $B^0 - \overline{B^0}$ mixing. However, it is difficult to observe it because of Equation (A.17) and $|M_{12}| \gg |\Gamma_{12}|$.

Time dependent CP asymmetry

From Equations (A.14) and (A.15), the time dependent CP asymmetry is,

$$
\begin{aligned}
Asy[f_{CP};t] &\equiv \frac{\Gamma(B^0(t) \to f_{CP}) - \Gamma(\overline{B^0}(t) \to f_{CP})}{\Gamma(B^0(t) \to f_{CP}) + \Gamma(\overline{B^0}(t) \to f_{CP})} \\
&= \frac{1}{1+|\rho|^2}\{2\mathrm{Im}\left(\frac{q}{p}\rho\right)\sin(\Delta M t) \\
&- (|\rho|^2 - 1)\cos(\Delta M t)\}, \qquad \text{(A.18)}
\end{aligned}
$$

where $\rho \equiv \langle f_{CP}|\overline{X^0}\rangle / \langle f_{CP}|X^0\rangle$.

Appendix B

Helix Fit

A helix parameter $\boldsymbol{a}$[5], that is, a representation of the spiral track, is calculated from axial and stereo hit wires, and a circle parameter is calculated from axial wires. For it, the least square method is used [1].

χ^2 is defined as

$$\chi^2 = \sum_{i=1}^{nhits} \left(\frac{\Delta_i}{\sigma_i}\right)^2$$

where

$$\begin{aligned}
\Delta_i &= d(\boldsymbol{x}_i(\phi_i)) - d_i \\
&= \sqrt{(x(\phi_i) - x_{wi})^2 + (y(\phi_i) - y_{wi})^2 + (z(\phi_i) - z_{wi})^2} - d_i \text{ (for stereo wires)} \\
&= \sqrt{(x(\phi_i) - x_{wi})^2 + (y(\phi_i) - y_{wi})^2} - d_i \text{ (for axial wires)}
\end{aligned}$$

d_i is a drift distance whose error is σ_i. The point $(x(\phi_i), y(\phi_i), z(\phi_i))$ on a helix or (x_{wi}, y_{wi}, z_{wi}) on a wire is the closest point between the helix and the wire.

This χ^2 is minimized using the Newton method. $d(\boldsymbol{x}_i)$ is a function of ϕ_i. Therefore Δ_i is a function of the helix parameter $\boldsymbol{a}$ and ϕ_i. The fitted helix parameter $\boldsymbol{a}$ can be numerically found by iteratively as following.

$$\boldsymbol{a}_{(D+1)} = \boldsymbol{a}_{(D)} - \left(\frac{\partial^2\chi^2}{\partial \boldsymbol{a}^T \partial \boldsymbol{a}}\right)^{-1}_{(D)} \left(\frac{\partial \chi^2}{\partial \boldsymbol{a}}\right)_{(D)}$$

where

$$\begin{aligned}
\boldsymbol{a} &= (d_\rho, \phi_0, \kappa, d_z, \tan\lambda)^T \\
\frac{\partial \chi^2}{\partial \boldsymbol{a}} &= 2 \sum_{i=1}^{nhits} \frac{1}{\sigma_i^2} \Delta_i \left(\frac{\partial \Delta_i}{\partial \boldsymbol{a}}\right) \\
\frac{\partial^2 \chi^2}{\partial \boldsymbol{a}^T \partial \boldsymbol{a}} &= 2 \sum_{i=1}^{nhits} \frac{1}{\sigma_i^2} \left\{\left(\frac{\partial \Delta_i}{\partial \boldsymbol{a}^T}\right)\left(\frac{\partial \Delta_i}{\partial \boldsymbol{a}}\right) + \Delta_i \frac{\partial^2 \Delta_i}{\partial \boldsymbol{a}^T \partial \boldsymbol{a}}\right\}
\end{aligned}$$

[1] The procedure is written in Reference [8] and I modified some parts.

$$
\begin{aligned}
&\simeq \quad 2\sum_{i=1}^{nhits}\frac{1}{\sigma_i^2}\{(\frac{\partial\Delta_i}{\partial \boldsymbol{a}^T})(\frac{\partial\Delta_i}{\partial \boldsymbol{a}})\} \qquad \text{(B.1)}\\
E_{\boldsymbol{a}} &= (\frac{1}{2}\frac{\partial^2\chi^2}{\partial\boldsymbol{a}^T\partial\boldsymbol{a}})^{-1}
\end{aligned}
$$

The second term in the first line of Equation (B.1) should be omitted to make the second derivative matrix of χ^2 positive definite[2]. $E_{\boldsymbol{a}}$ is an error of the helix parameter $\boldsymbol{a}$.

It is necessary to calculate $\frac{\partial\Delta_i}{\partial\boldsymbol{a}}$. $\boldsymbol{x}_w$ is Equation (B.3) and this is a function of ϕ_i.

$$
\frac{\partial\Delta_i}{\partial\boldsymbol{a}} = \frac{X\frac{\partial x(\phi_i)}{\partial\boldsymbol{a}} + Y\frac{\partial y(\phi_i)}{\partial\boldsymbol{a}} + Z\frac{\partial z(\phi_i)}{\partial\boldsymbol{a}}}{\sqrt{(x(\phi_i)-x_{wi})^2+(y(\phi_i)-y_{wi})^2+(z(\phi_i)-z_{wi})^2}}
$$

$$
\begin{aligned}
X &\equiv (x(\phi_i)-x_{wi})(1-v_x^2) - (y(\phi_i)-y_{wi})v_xv_y - (z(\phi_i)-z_{wi})v_xv_z\\
Y &\equiv (y(\phi_i)-y_{wi})(1-v_y^2) - (z(\phi_i)-z_{wi})v_yv_z - (x(\phi_i)-x_{wi})v_yv_x\\
Z &\equiv (z(\phi_i)-z_{wi})(1-v_z^2) - (x(\phi_i)-x_{wi})v_zv_x - (y(\phi_i)-y_{wi})v_zv_y\\
\frac{\partial x}{\partial d_\rho} &= \cos\phi_0 + \frac{\alpha}{\kappa}\sin(\phi_0+\phi_i)\frac{\partial\phi_i}{\partial d_\rho}\\
\frac{\partial x}{\partial \phi_0} &= -\left(d_\rho+\frac{\alpha}{\kappa}\right)\sin\phi_0 + \frac{\alpha}{\kappa}\sin(\phi_0+\phi_i)\left(1+\frac{\partial\phi_i}{\partial\phi_0}\right)\\
\frac{\partial x}{\partial \kappa} &= -\frac{\alpha}{\kappa^2}\{\cos\phi_0-\cos(\phi_0+\phi_i)\} + \frac{\alpha}{\kappa}\sin(\phi_0+\phi_i)\frac{\partial\phi_i}{\partial\kappa}\\
\frac{\partial x}{\partial d_z} &= \frac{\alpha}{\kappa}\sin(\phi_0+\phi_i)\frac{\partial\phi_i}{\partial d_z}\\
\frac{\partial x}{\partial \tan\lambda} &= \frac{\alpha}{\kappa}\sin(\phi_0+\phi_i)\frac{\partial\phi_i}{\partial\tan\lambda}\\
\frac{\partial y}{\partial d_\rho} &= \sin\phi_0 - \frac{\alpha}{\kappa}\cos(\phi_0+\phi_i)\frac{\partial\phi_i}{\partial d_\rho}\\
\frac{\partial y}{\partial \phi_0} &= \left(d_\rho+\frac{\alpha}{\kappa}\right)\cos\phi_0 - \frac{\alpha}{\kappa}\cos(\phi_0+\phi_i)\left(1+\frac{\partial\phi_i}{\partial\phi_0}\right)\\
\frac{\partial y}{\partial \kappa} &= -\frac{\alpha}{\kappa^2}\{\sin\phi_0-\sin(\phi_0+\phi_i)\} - \frac{\alpha}{\kappa}\cos(\phi_0+\phi_i)\frac{\partial\phi_i}{\partial\kappa}\\
\frac{\partial y}{\partial d_z} &= -\frac{\alpha}{\kappa}\cos(\phi_0+\phi_i)\frac{\partial\phi_i}{\partial d_z}\\
\frac{\partial y}{\partial \tan\lambda} &= -\frac{\alpha}{\kappa}\cos(\phi_0+\phi_i)\frac{\partial\phi_i}{\partial\tan\lambda}\\
\frac{\partial z}{\partial d_\rho} &= -\frac{\alpha}{\kappa}\tan\lambda\frac{\partial\phi_i}{\partial d_\rho}
\end{aligned}
$$

[2]This term would be ignored at the χ^2 minimum since the residual Δ_i could be small if the spatial resolution of the detector is good enough. And more exact calculation of the charged tracks is done by Kalman Filtering Technique, because multiple scattering , energy loss, and so on are considered in the local position of the helix.

$$
\begin{aligned}
\frac{\partial z}{\partial \phi_0} &= -\frac{\alpha}{\kappa}\tan\lambda\frac{\partial \phi_i}{\partial \phi_0} \\
\frac{\partial z}{\partial \kappa} &= \frac{\alpha}{\kappa}\tan\lambda(\frac{\phi_i}{\kappa} - \frac{\partial \phi_i}{\partial \kappa}) \\
\frac{\partial z}{\partial d_z} &= 1 - \frac{\alpha}{\kappa}\tan\lambda\frac{\partial \phi_i}{\partial d_z} \\
\frac{\partial z}{\partial \tan\lambda} &= -\frac{\alpha}{\kappa}\left(\phi_i + \tan\lambda\frac{\partial \phi_i}{\partial \tan\lambda}\right)
\end{aligned}
$$

In the case of axial wires, the components associated with z must be ignored.

Next, for these equations, it is necessary to calculate the closest point between the helix and each wire, and $\frac{\partial \phi_i}{\partial \boldsymbol{a}}$.

B.1 Calculation of The Closest Point from Helix to Each Wire and $\partial\phi_i/\partial\boldsymbol{a}$

The closest point from helix to each axial wire can be calculated easily, but in case of stereo wires, it is necessary to use the Newton Method.

To obtain the closest point is the same with obtaining ϕ_i. Using them, $\frac{\partial \phi_i}{\partial \boldsymbol{a}}$ can be calculated.

The closest point in case of axial wires is obtained by [3]

$$
\tan(\phi_0 + \phi_i) = \frac{\frac{\alpha}{\kappa}(y_c - y_{wi})}{\frac{\alpha}{\kappa}(x_c - x_{wi})} \tag{B.2}
$$

where

$$
\begin{aligned}
x_c &= x_0 + (d_\rho + \frac{\alpha}{\kappa})\cos\phi_0 \\
y_c &= y_0 + (d_\rho + \frac{\alpha}{\kappa})\sin\phi_0.
\end{aligned}
$$

From Equation (B.2), $\frac{\partial \phi_i}{\partial \boldsymbol{a}}$ is derived as

$$
\begin{aligned}
\frac{\partial \phi_i}{\partial d_\rho} &= \frac{\sin\phi_0(x_c - x_{wi}) - \cos\phi_0(y_c - y_{wi})}{(x_c - x_{wi})^2 + (y_c - y_{wi})^2} \\
\frac{\partial \phi_i}{\partial \phi_0} &= \left(d_\rho + \frac{\alpha}{\kappa}\right)\left(\frac{\cos\phi_0(x_c - x_{wi}) + \sin\phi_0(y_c - y_{wi})}{(x_c - x_{wi})^2 + (y_c - y_{wi})^2}\right) - 1 \\
\frac{\partial \phi_i}{\partial \kappa} &= \left(-\frac{\alpha}{\kappa^2}\right)\left(\frac{\sin\phi_0(x_c - x_{wi}) - \cos\phi_0(y_c - y_{wi})}{(x_c - x_{wi})^2 + (y_c - y_{wi})^2}\right)
\end{aligned}
$$

Next, the Newton Method is necessary for determination of the closest point from helix to each stereo wire. D that is the square of the distance between helix track and wire, is defined as

$$
D \equiv |\boldsymbol{x}(\phi) - \boldsymbol{x}_w|^2
$$

[3] $\frac{\alpha}{\kappa}$ is needed to write the program, because `atan2` of the math library is used.

where,

$$
\begin{aligned}
F &\equiv -D/2 \\
\boldsymbol{x}_w &= \boldsymbol{x}_b + \{(\boldsymbol{x}(\phi) - \boldsymbol{x}_b) \cdot \boldsymbol{v}^T\}\boldsymbol{v} \\
&= \boldsymbol{c} + (\boldsymbol{x}(\phi) \cdot \boldsymbol{v}^T)\boldsymbol{v} \\
\boldsymbol{c} &\equiv \boldsymbol{x}_b - (\boldsymbol{x}_b \cdot \boldsymbol{v}^T)\boldsymbol{v}
\end{aligned} \tag{B.3}
$$

$\boldsymbol{x}(\phi)$ represents a helix track. $\boldsymbol{x}_w$ represents position of the wire. $\boldsymbol{x}_b$ represents the backward wire position of the CDC endplate. $\boldsymbol{v}$ represents the directional unit vector of the wire.

$f \equiv \frac{\partial F}{\partial \phi}$ and $df \equiv \frac{\partial f}{\partial \phi} = \frac{\partial^2 F}{\partial \phi^2}$ are calculated. And if $f \geq 10^{-5}$, ϕ_{new} is calculated by $\phi_{new} = \phi_{old} - \frac{f}{df}$ and calculates again.

Some equations are written in detail as follows.

$$
\begin{aligned}
f &\equiv \frac{\partial F}{\partial \phi} \\
&= -(\boldsymbol{x}(\phi) - \boldsymbol{x}_w) \cdot \frac{\partial \boldsymbol{x}(\phi)^T}{\partial \phi} + (\boldsymbol{x}(\phi) - \boldsymbol{x}_w) \cdot \frac{\partial \boldsymbol{x}_w^T}{\partial \phi} \\
&= -(\boldsymbol{x}(\phi) - \boldsymbol{x}_w + (\boldsymbol{c} \cdot \boldsymbol{v}^T)\boldsymbol{v}) \cdot \frac{\partial \boldsymbol{x}(\phi)^T}{\partial \phi} \\
&= -(\boldsymbol{x}(\phi) - \boldsymbol{x}_w) \cdot \frac{\partial \boldsymbol{x}(\phi)^T}{\partial \phi} \\
&= -(\boldsymbol{x}(\phi) - \boldsymbol{c} - (\boldsymbol{x}(\phi) \cdot \boldsymbol{v}^T)\boldsymbol{v}) \cdot \frac{\partial \boldsymbol{x}(\phi)^T}{\partial \phi}
\end{aligned} \tag{B.4}
$$

$\boldsymbol{v} \cdot \boldsymbol{v}^T = 1, \boldsymbol{c} \cdot \boldsymbol{v}^T = 0$ are used here.

$$
\begin{aligned}
\frac{\partial f}{\partial \phi} &\equiv \frac{\partial^2 F}{\partial \phi^2} \\
&= -\frac{\partial \boldsymbol{x}(\phi)}{\partial \phi} \cdot \frac{\partial \boldsymbol{x}(\phi)^T}{\partial \phi} + (\frac{\partial \boldsymbol{x}(\phi)}{\partial \phi} \cdot \boldsymbol{v}^T)^2 \\
&- (\boldsymbol{x}(\phi) - \boldsymbol{c} - (\boldsymbol{x}(\phi) \cdot \boldsymbol{v}^T)\boldsymbol{v})\frac{\partial^2 \boldsymbol{x}(\phi)^T}{\partial \phi^2}
\end{aligned} \tag{B.5}
$$

$\boldsymbol{x}$ is necessary for the calculation of these equations.

$$
\begin{aligned}
x &= x_0 + d_\rho \cos\phi_0 + \frac{\alpha}{\kappa}(\cos\phi_0 - \cos(\phi_0 + \phi)) \\
y &= y_0 + d_\rho \sin\phi_0 + \frac{\alpha}{\kappa}(\sin\phi_0 - \sin(\phi_0 + \phi)) \\
z &= z_0 + d_z - \frac{\alpha}{\kappa}\tan\lambda \cdot \phi
\end{aligned}
$$

$$
\begin{aligned}
\frac{\partial x}{\partial \phi} &= \frac{\alpha}{\kappa}\sin(\phi_0 + \phi), \quad \frac{\partial y}{\partial \phi} = -\frac{\alpha}{\kappa}\cos(\phi_0 + \phi), \quad \frac{\partial z}{\partial \phi} = -\frac{\alpha}{\kappa}\tan\lambda \\
\frac{\partial^2 x}{\partial \phi^2} &= \frac{\alpha}{\kappa}\cos(\phi_0 + \phi), \quad \frac{\partial^2 y}{\partial \phi^2} = \frac{\alpha}{\kappa}\sin(\phi_0 + \phi), \quad \frac{\partial^2 z}{\partial \phi^2} = 0
\end{aligned} \tag{B.6}
$$

From these equations, ϕ_i is obtained by the Newton Method. Next, $\frac{\partial \phi_i}{\partial \boldsymbol{a}}$ is calculated as follows.

$$
\begin{aligned}
\frac{\partial f}{\partial \boldsymbol{a}} &= \left(\frac{\partial f}{\partial \phi_i}\right)\left(\frac{\partial \phi_i}{\partial \boldsymbol{a}}\right) + \frac{\partial f}{\partial \boldsymbol{a}}\Big|_{\phi_i \text{is fixed}} \\
&= 0 \\
\frac{\partial \phi_i}{\partial \boldsymbol{a}} &= -\frac{\frac{\partial f}{\partial \boldsymbol{a}}\big|_{\phi_i \text{is fixed}}}{\frac{\partial f}{\partial \phi_i}}
\end{aligned}
$$

$\frac{\partial f}{\partial \phi_i}$ is Equation (B.5). To obtain it, let us calculate following equations.

$$
\begin{aligned}
\frac{\partial x}{\partial \phi_i} &= \frac{\alpha}{\kappa}\sin(\phi_0+\phi_i), \quad \frac{\partial y}{\partial \phi_i} = -\frac{\alpha}{\kappa}\cos(\phi_0+\phi_i), \quad \frac{\partial z}{\partial \phi_i} = -\frac{\alpha}{\kappa}\tan\lambda \\
\frac{\partial^2 x}{\partial \phi_i^2} &= \frac{\alpha}{\kappa}\cos(\phi_0+\phi_i), \quad \frac{\partial^2 y}{\partial \phi_i^2} = \frac{\alpha}{\kappa}\sin(\phi_0+\phi_i), \quad \frac{\partial^2 z}{\partial \phi_i^2} = 0
\end{aligned}
$$

To obtain $\frac{\partial f}{\partial \boldsymbol{a}}$, let us calculate Equation (B.4) as follows. In this calculation, ϕ_i is fixed.

$$
\frac{\partial f}{\partial \boldsymbol{a}}\Big|_{\phi_i \text{is fixed}} = -\left(\frac{\partial \boldsymbol{x}}{\partial \boldsymbol{a}} - \left(\frac{\partial \boldsymbol{x}}{\partial \boldsymbol{a}}\cdot \boldsymbol{v}^T\right)\boldsymbol{v}\right)\frac{\partial \boldsymbol{x}^T}{\partial \phi} - (\boldsymbol{x} - \boldsymbol{c} - (\boldsymbol{x}\cdot\boldsymbol{v}^T)\boldsymbol{v})\frac{\partial^2 \boldsymbol{x}^T}{\partial \boldsymbol{a}\partial \phi}
$$

$$
\begin{aligned}
\frac{\partial^2 x}{\partial d_\rho \partial \phi_i} &= 0, \quad \frac{\partial^2 x}{\partial \phi_0 \partial \phi_i} = \frac{\alpha}{\kappa}\cos(\phi_0+\phi_i) \\
\frac{\partial^2 x}{\partial \kappa \partial \phi_i} &= -\frac{\alpha}{\kappa^2}\sin(\phi_0+\phi_i), \quad \frac{\partial^2 x}{\partial d_z \partial \phi_i} = 0, \quad \frac{\partial^2 x}{\partial \tan\lambda \partial \phi_i} = 0 \\
\frac{\partial^2 y}{\partial d_\rho \partial \phi_i} &= 0, \quad \frac{\partial^2 y}{\partial \phi_0 \partial \phi_i} = \frac{\alpha}{\kappa}\sin(\phi_0+\phi_i) \\
\frac{\partial^2 y}{\partial \kappa \partial \phi_i} &= \frac{\alpha}{\kappa^2}\cos(\phi_0+\phi_i), \quad \frac{\partial^2 y}{\partial d_z \partial \phi_i} = 0, \quad \frac{\partial^2 y}{\partial \tan\lambda \partial \phi_i} = 0 \\
\frac{\partial^2 z}{\partial d_\rho \partial \phi_i} &= 0, \quad \frac{\partial^2 z}{\partial \phi_0 \partial \phi_i} = 0, \quad \frac{\partial^2 z}{\partial \kappa \partial \phi_i} = \frac{\alpha}{\kappa^2}\tan\lambda \\
\frac{\partial^2 z}{\partial d_z \partial \phi_i} &= 0, \quad \frac{\partial^2 z}{\partial \tan\lambda \partial \phi_i} = -\frac{\alpha}{\kappa} \\
\frac{\partial x}{\partial d_\rho} &= \cos\phi_0, \quad \frac{\partial x}{\partial \phi_0} = -(d_\rho + \frac{\alpha}{\kappa})\sin\phi_0 + \frac{\alpha}{\kappa}\sin(\phi_0+\phi_i) \\
\frac{\partial x}{\partial \kappa} &= -\frac{\alpha}{\kappa^2}(\cos\phi_0 - \cos(\phi_0+\phi_i)), \quad \frac{\partial x}{\partial d_z} = 0, \quad \frac{\partial x}{\partial \tan\lambda} = 0 \\
\frac{\partial y}{\partial d_\rho} &= \sin\phi_0, \quad \frac{\partial y}{\partial \phi_0} = (d_\rho + \frac{\alpha}{\kappa})\cos\phi_0 - \frac{\alpha}{\kappa}\cos(\phi_0+\phi_i) \\
\frac{\partial y}{\partial \kappa} &= -\frac{\alpha}{\kappa^2}(\sin\phi_0 - \sin(\phi_0+\phi_i)), \quad \frac{\partial y}{\partial d_z} = 0, \quad \frac{\partial y}{\partial \tan\lambda} = 0
\end{aligned}
$$

$$
\begin{aligned}
\frac{\partial z}{\partial d_\rho} &= 0, \quad \frac{\partial z}{\partial \phi_0} = 0, \quad \frac{\partial z}{\partial \kappa} = \frac{\alpha}{\kappa^2} \tan\lambda \cdot \phi_i \\
\frac{\partial z}{\partial d_z} &= 1, \quad \frac{\partial z}{\partial \tan\lambda} = -\frac{\alpha}{\kappa} \phi_i
\end{aligned}
$$

Appendix C

The Simulation and The Reconstruction Programs in BELLE

The flow of the physics analysis is as follows.

Event Generation $\rightarrow$ Detector Simulation $\rightarrow$ Reconstruction $\rightarrow$ Analysis

There exist two ways for our physics analysis in BELLE. One is event generator(QQ[10]) + fast simulator(FSIM[11]) + analysis softwares and the other is QQ + full detector simulator(GSIM) + reconstruction softwares + analysis softwares.

FSIM is a fast simulator. It plays the role of the detector simulation and reconstruction softwares. In FSIM, all effects of detectors are parameterized as track reconstruction efficiencies and probabilities of particle identifications etc, so that, we can analyze many events($10^{7\sim8}$) easily. FSIM is necessary for large background studies.

GSIM is a full simulator and its base is GEANT3[12]. In GSIM, all effects of detectors are calculated step by step obeying information of their geometries and materials, so that, we need much time to analyze many events. And a track reconstruction and particle identifications etc. are not done in GSIM. Therefore reconstruction softwares are necessary for the track reconstruction and particle identifications. They are made by detector-groups. The low momentum track reconstruction program is one of them. GSIM is necessary to obtain efficiencies of signals and for $10^{4\sim5}$ background studies.

Finally, we need our physics analysis softwares after FSIM or GSIM. Combination of particles and mass reconstructions etc. are performed in them. The kinematic fitter is necessary in this stage.

Bibliography

[1] M.Kobayashi and T.Masukawa, Prog.Theor.Phys.**49** 652 (1973)

[2] A.B.Carter and A.I.Sanda, Phys.Rev.Lett.**45** 952 (1980), Phys.Rev.**D23** 1567 (1981)

[3] BELLE Technical Design Report, KEK Report 95-1

[4] J.H.Christenson, J.W.Cronin, V.L.Fitch and R.Turlay Phys.Rev.Lett.**13** 138 (1964)

[5] Track Parameterization (Y.Ohnishi) BELLE Note #148

[6] Applied Fitting Theory I,IV,VI(Paul Avery)

[7] Kinematic Fitting (J.Tanaka) BELLE Note #194

[8] Fast Tracker For the Drift Chamber (J.Tanaka) BELLE Note #222

[9] Research and Development of the B-Factory High Precision Central Drift Chamber with Capability of Particle Identification (K.Tsukamoto) Doctor Thesis (1996)

[10] QQ Quick Reference for BELLE (R.Itoh) (1995)

[11] FSIM V5.0 (H.Ozaki) BELLE Note #99

[12] GEANT CERN Program Library Long Writeup W5013

[13] Calculation of Track and Vertex Errors for Detector Design Studies Robert Harr IEEE Trans.Nucl.Sci.,vol. 42, pp.134-147, June 1995